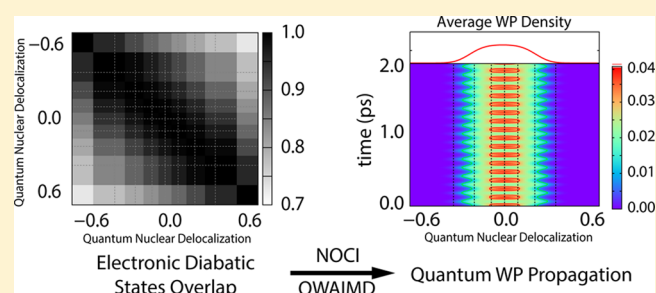# Vibrational Properties of Hydrogen-Bonded Systems Using the Multireference Generalization to the "On-the-Fly" Electronic Structure within Quantum Wavepacket ab Initio Molecular Dynamics (QWAIMD)

Junjie Li, Xiaohu Li, and Srinivasan S. Iyengar*

Department of Chemistry and Department of Physics, Indiana University, 800 East Kirkwood Avenue, Bloomington, Indiana 47405, United States

ABSTRACT: We discuss a multiconfigurational treatment of the "on-the-fly" electronic structure within the quantum wavepacket ab initio molecular dynamics (QWAIMD) method for coupled treatment of quantum nuclear effects with electronic structural effects. Here, multiple single-particle electronic density matrices are simultaneously propagated with a quantum nuclear wavepacket and other classical nuclear degrees of freedom. The multiple density matrices are coupled through a nonorthogonal configuration interaction (NOCI) procedure to construct the instantaneous potential surface. An adaptive-mesh-guided set of basis functions composed of Gaussian primitives are used to simplify the electronic structure calculations. Specifically, with the replacement of the atom-centered basis functions positioned on the centers of the quantum-mechanically treated nuclei by a mesh-guided band of basis functions, the two-electron integrals used to compute the electronic structure potential surface become independent of the quantum nuclear variable and hence reusable along the entire Cartesian grid representing the quantum nuclear coordinates. This reduces the computational complexity involved in obtaining a potential surface and facilitates the interpretation of the individual density matrices as representative diabatic states. The parametric nuclear position dependence of the diabatic states is evaluated at the initial time-step using a Shannon-entropy-based sampling function that depends on an approximation to the quantum nuclear wavepacket and the potential surface. This development is meant as a precursor to an on-the-fly fully multireference electronic structure procedure embedded, on-the-fly, within a quantum nuclear dynamics formalism. We benchmark the current development by computing structural, dynamic, and spectroscopic features for a series of bihalide hydrogen-bonded systems: FHF⁻, ClHCl⁻, BrHBr⁻, and BrHCl⁻. We find that the donor–acceptor structural features are in good agreement with experiments. Spectroscopic features are computed using a unified velocity/flux autocorrelation function and include vibrational fundamentals and combination bands. These agree well with experiments and other theories.

I. INTRODUCTION

Quantum nuclear effects have a critical role in several systems. These include many hydrogen transfer reactions occurring inside enzyme complexes[1] and classic cases of hydrogen transfer known in physical organic chemistry.[2,3] In addition, hydrogen-bonded clusters may display quantum nuclear effects that govern the vibrational properties of the shared hydrogen atom.[4–9] To compute these important effects, we introduced an approach called quantum wavepacket ab initio molecular dynamics (QWAIMD).[4,10–19] The goal of QWAIMD is to study the quantum dynamical effects in a subsystem, such as the shared proton in a hydrogen-bonded system,[4,15] or the transferring hydrogen atom in a reaction,[17,20,21] while simultaneously treating the dynamics of the surrounding particles along with the coupled changes in electronic structure. The approach is quantum-classical[22–33] and involves the synergy between a time-dependent quantum wavepacket description and ab initio molecular dynamics. Because the quantum dynamics within

QWAIMD is generally performed on a grid, the predominant bottleneck is the calculation of the grid-based, time-dependent electronic structure potential and gradients generated from the motion of the classical particles. In refs 4, 12, and 16, this limitation was handled through introduction of an adaptive, space–time-dependent, mesh refinement scheme called the time-dependent deterministic sampling (TDDS),[4,12] which shares common features with the h-type mesh refinement procedure known in computational fluid dynamics.[34] The TDDS method when combined with numerical techniques such as an efficient wavelet compression scheme[35–42] and low-pass filtered Lagrange interpolation, provides computational gains of several orders of magnitude. The QWAIMD approach has been used to study vibrational properties in hydrogen-bonded clusters inclusive of quantum nuclear effects,[4] hydrogen tunneling in

Table 1. Vibrational Frequencies for Cl−H−Cl$^-$ (ν_3 = Shared Proton Stretch)

	level of theory	ν_1 (cm^{-1})	ν_2 (cm^{-1})		ν_3 (cm^{-1})	
harmonic approximation	B3LYP/6-31+G(d,p)	328	834[a]	849[b]	560[a]	949[b]
	MP2/6-31+G(d,p)	353	893[a]	907[b]	98[a]	865[b]
	B3LYP/aug-cc-pVTZ	324	818[a]	829[b]	582[a]	952[b]
	MP2/aug-cc-pVTZ	345	847[a]	863[b]	637[a]	974[b]
	CCSD/aug-cc-pVTZ	181	828[a]	874[b]	833[a]	764[b]
	CCSD(T)/aug-cc-pVTZ	340	842[a]		325[a]	
1D a-QWAIMD[c]	B3LYP/6-31+G(d,p)[d]	301			988	
	B3LYP/6-31+G(d,p)[e]	297			900	
	MP2/6-31+G(d,p)[f]	313			879	
	MP2/6-31+G(d,p)[g]	304			746	
3D a-QWAIMD[c]	B3LYP/6-31+G*[h]	300	857		806	
	B3LYP/6-31+G*[i]	254	863		723	
experiment [ref 43]		318	792 ± 9		723	
NEO-MP2(ee+ep) [ref 5]		334				
CC-VSCF-MP2 [ref 5]		327	811		925	

[a]Harmonic frequencies corresponding to the optimized geometry. [b]Obtained from three-dimensional $0 \rightarrow 1$ eigenstate transitions. The potential energy surface for the eigenstates is obtained from a full-scan of the quantum proton, with the chlorine atoms fixed at optimized geometry positions. Hence, the eigenstates here are corrected for the true anharmonicity at that geometry but do not include coupling with the chlorine atom distribution, which would dynamically perturb the anharmonicity. Note the large changes already present though. For example, see MP2/6-31+G(d,p) in comparison with the ν_3 frequency at the optimized geometry. [c]Calculated using the flux/velocity correlation function introduced in ref 4 and presented here in eq 8. The trajectories are computed using a-QWAIMD. [d]Average internal kinetic energy corresponding to a temperature of 133.76 K. [e]Average internal kinetic energy corresponding to a temperature of 271.14 K. [f]Average internal kinetic energy corresponding to a temperature of 127.26 K. [g]Average internal kinetic energy corresponding to a temperature of 290.17 K. [h]Average internal kinetic energy corresponding to a temperature of 323.50 K. [i]Average internal kinetic energy corresponding to a temperature of 714.45 K.

enzyme active sites[17] and quantum nuclear effects in solid state protonic conductors.[15] The quantum dynamics scheme in QWAIMD has also been adopted to develop a technique known as multistage ab initio wavepacket dynamics (MSAIWD)[18,19] to treat the electronic structure and dynamics in open, nonequilibrium systems such as those encountered in molecular wires.

In ref 14, a multiconfigurational generalization to QWAIMD was presented to accurately depict the coupling between quantum nuclear degrees of freedom and the electronic structure. In this publication, we benchmark the multiconfigurational QWAIMD approach. For notational simplicity, the multiconfigurational generalization to QWAIMD is referred to as MC-QWAIMD and the previous implementation discussed in ref 4 is called adiabatic QWAIMD or a-QWAIMD. The specific systems studied here are hydrogen-bonded clusters that are represented as XHY^{-1}, where the atoms X and Y are both halogen atoms. These systems contain a shared proton undergoing excursions along the donor−acceptor axis. The motion of the proton is (a) coupled to the two peripheral atoms, and (b) dictated by the highly anharmonic nature of the potential surfaces.[4] In fact, as noted in ref 4, the anharmonic contributions are significant for ClHCl$^-$, and borrowing the standard diatomic molecular spectroscopy notation,[44] the first-order anharmonic constant, $w_e x_e$, is negative because the spacing between adjacent vibrational levels increases, implying quartic and higher order contributions to the surface. (See Table 5 in ref 4.) Furthermore, there is substantial red shift in the proton stretch frequency when the coupled motion of the peripheral atoms is included. These aspects make the problem challenging not only for the commonly utilized harmonic analysis constructed at optimized geometries but also for many state-of-art methods such as the nuclear electronic orbital approach constructed at the MP2 level,[5] and the CC-VSCF-MP2[5,45−48] method. In our previous work, we showed that the vibrational density of states obtained from a-QWAIMD,[4] obtained using a velocity-wavepacket-flux autocorrelation function, is able to provide quantitative agreement with experimental results (Table 1). As a result, in an effort to benchmark the multiconfigurational generalization to QWAIMD, we compare our energetic and dynamical features obtained from MC-QWAIMD simulations with those obtained from the a-QWAIMD as well as those obtained from gas-phase spectroscopy experiments[43,49−58] and other theories.[5,59]

Salient features of MC-QWAIMD are as follows: Multiple single-particle electronic density matrices are simultaneously propagated along with the quantum nuclear wavepacket. The multiple density matrices are chosen such that the corresponding electronic wave functions have minimal dependence on the quantum nuclear coordinates, and hence these are akin to diabatic states.[60−67] These states are then used within non-orthogonal configuration interaction (NOCI)[14,68−76] to construct on-the-fly, adiabatic, potential surfaces that may be valid beyond the single particle approximation, depending on the choice of the single particle functions. In addition, the "on-the-fly" potential surface calculations differ from those standardly used in quantum chemistry because a combination of atom-centered Gaussians and an *adaptive-mesh-guided set of Gaussian basis functions* are used here. Specifically, the atom-centered Gaussian basis functions that depend on the quantum-nuclear coordinates are eliminated in favor of a set of Gaussian basis functions that are placed on a three-dimensional adaptive mesh. The mesh itself adapts to the position of the other classically treated nuclei. This allows us to eliminate the two-electron integral dependence on the quantum nuclear degrees of freedom thus making them reusable over the entire quantum nuclear grid to reduce computational cost.

The paper is organized as follows: In section II, the MC-QWAIMD method is briefly summarized, with some technical details provided in Appendices A and B. Results from calculations on the chosen hydrogen-bonded systems are discussed in section III with conclusions in section IV.
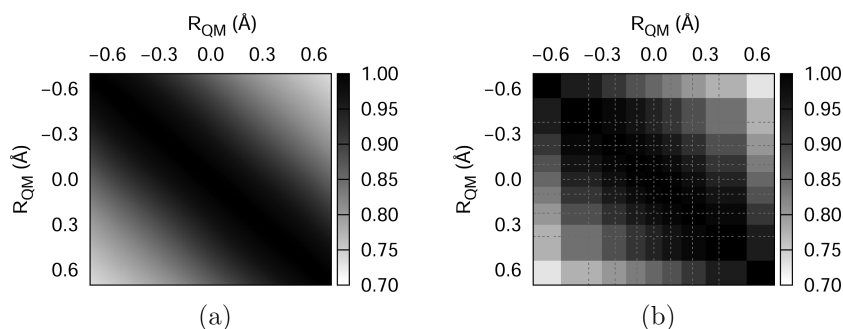
Figure 1. Morphology of the overlap matrix in eq 2. The horizontal and vertical axes in each case indicate progress along the quantum nuclear grid. The grid points that are in close proximity register a greater overlap for the quantity in eq 2 as indicated by the darker regions close to the diagonal. This figure also demonstrates the "local" nature of the diabatic states in the quantum nuclear representation. That is, the diabatic states $\Phi_I^{(\text{diab})}$, which are uniquely determined at the nuclear configuration $\{\mathbf{R}_C; R_{\text{QM}}^{I*}\}$, are similar when the respective R_{QM}^{I*} values are close. (a) represents the continuous case, where an extremely large number of diabatic states have been used, equal to the number of quantum nuclear grid points, whereas (b) is the case for nine diabatic states. (The respective R_{QM}^{I*} positions are shown using gray dotted lines in (b).) For reference, when the overlap is 0.9, the hyper-angle in Hilbert space between the two vectors $\Phi_I^{(\text{diab})}$ and $\Phi_J^{(\text{diab})}$ is 25.8°. Similarly, when the overlap is 0.7, the hyper-angle is 45.6°. Hence these diabatic states are dissimilar and are used here as reference states for the electronic wave function at each quantum nuclear grid point.

II. MULTICONFIGURATIONAL EXTENSIONS TO THE ON-THE-FLY ELECTRONIC STRUCTURE TREATMENT IN QWAIMD

A. Summary of MC-QWAIMD. The quantum nuclear dynamical procedure used in QWAIMD has been well-reviewed in several publications.[10,11,15,18] Here, we summarize the multiconfigurational approach to determine the on-the-fly adiabatic electronic surface used for quantum nuclear dynamics. The adiabatic electronic structure, $\Psi_{\text{el}}^{(n)}$, is written as a multiconfigurational expansion of local, single particle state functions, $\{\Phi_I^{(\text{diab})}\}$, as

$$\Psi_{\text{el}}^{(n)}(\mathbf{r}_{\text{el}}, \mathbf{R}_{\text{QM}}, \mathbf{R}_C; t)$$
$$= \sum_I c_I^{(n)}(\mathbf{R}_{\text{QM}}, \mathbf{R}_C; t)\Phi_I^{(\text{diab})}(\mathbf{R}_C, \mathbf{r}_{\text{el}}; t) \tag{1}$$

Here, the quantities $\mathbf{R}_{\text{QM}}$, $\mathbf{R}_C$, and $\mathbf{r}_{\text{el}}$ are the quantized nuclear coordinates, the classically treated nuclear degrees of freedom and electronic coordinates, respectively. As explicitly noted, the multiconfigurational coefficients $c_I^{(n)}$ depend on both the quantum nuclear degrees of freedom, $\mathbf{R}_{\text{QM}}$, and the classical nuclear positions, $\mathbf{R}_C$. The state functions, $\{\Phi_I^{(\text{diab})}\}$, in turn depend parametrically on the classical nuclear positions $\mathbf{R}_C$ and are chosen to have no explicit dependence on the quantum nuclear degrees of freedom. In this sense, $\{\Phi_I^{(\text{diab})}\}$, may be interpreted as diabatic functions,[60–67] i.e., states with zero velocity coupling through the quantum nuclear momentum operator and $\langle\Phi_I^{(\text{diab})}|\nabla_{\mathbf{R}_{\text{QM}}}|\Phi_J^{(\text{diab})}\rangle = 0$. That is, the momentum coupling is zero with respect to the quantum nuclear degrees of freedom.[70,71,73,77–81] *Hence, $\{\Phi_I^{(\text{diab})}\}$ are subspace-diabatic, where the diabaticity is only limited to a subset of nuclear degrees of freedom depicted by $\mathbf{R}_{\text{QM}}$ and not with respect to $\mathbf{R}_C$.* We further require that each $\Phi_I^{(\text{diab})}$ represent the local electronic structure within the quantum nuclear basis domain. That is, $\Phi_I^{(\text{diab})}$ is to represent the electronic structure for nuclear configurations in the neighborhood of $\{R_{\text{QM}}^{I*}; \mathbf{R}_C\}$.[14] Here, R_{QM}^{I*} is a position on the quantum grid that uniquely determines $\Phi_I^{(\text{diab})}$. [In Appendix B1, we provide a deterministic sampling algorithm that allows us to obtain R_{QM}^{I*} at the initial step.] Hence, the states, $\Phi_I^{(\text{diab})}$, are akin to "valence-bond" states.[77–81] A family of such states, $\{\Phi_I^{(\text{diab})}\}$, are then used to expand the electronic wavefunction as indicated in eq 1.

A given diabatic state function, $\Phi_I^{(\text{diab})}$, is expressed as a Slater determinant composed of one electron functions $\{|\chi_i^I\rangle\}$. These one-electron functions are in general nonorthogonal and hence the Slater determinants are nonorthogonal according to

$$\langle\Phi_I^{(\text{diab})}|\Phi_J^{(\text{diab})}\rangle = S_{I,J} = \det[s^{I,J}] \tag{2}$$

where

$$s^{I,J} = \begin{bmatrix} \langle\chi_1^I|\chi_1^J\rangle & \cdots & \langle\chi_N^I|\chi_1^J\rangle \\ \vdots & \vdots & \vdots \\ \langle\chi_1^I|\chi_N^J\rangle & \cdots & \langle\chi_N^I|\chi_N^J\rangle \end{bmatrix} \tag{3}$$

is a nonsymmetric matrix. The locality of the electronic structure functions, $\{\Phi_I^{(\text{diab})}\}$, in the $\mathbf{R}_{\text{QM}}$ domain, is depicted through illustration of the overlap, eq 2, in Figure 1.

The time dependence of the diabatic states, $\{\Phi_I^{(\text{diab})}\}$, is approximated as follows: The functions $\{|\chi_i^I\rangle\}$ are used to construct the single electron density matrices, $\{\mathbf{P}_I\}$, which, along with the classical nuclear degrees of freedom $\mathbf{R}_C$, are propagated using the multiple diabatic state extended Lagrangian,

$$\mathcal{L} = \frac{1}{2}\text{Tr}[\mathbf{V}_C^T\mathbf{M}_C\mathbf{V}_C] + \sum_I^{N_{\text{DM}}} \frac{1}{2}\text{Tr}[(\mu_I^{1/4}\mathbf{W}_I\mu_I^{1/4})^2]$$
$$- E(\mathbf{R}_C, \{\mathbf{P}_I\}, \mathbf{R}_{\text{QM}}) - \sum_I^{N_{\text{DM}}} \text{Tr}[\Lambda_I(\mathbf{P}_I^2 - \mathbf{P}_I)] \tag{4}$$

Here, $\mathbf{M}_C$ and $\mathbf{V}_C$ are the classical nuclear masses and velocities respectively, whereas $\mathbf{W}_I$ and μ_I are the diabatic density matrix velocity and tensorial fictitious mass, respectively. The scalar quantity, N_{DM}, represents the number of density matrices (or diabatic states). Equation 4 is an extension of the classical Lagrangian used in atom-centered density matrix propagation (ADMP)[82–85] but differs through (a) the use of multiple single particle density matrix trajectories and (b) the energy $E(\mathbf{R}_C, \{\mathbf{P}_I\}, \mathbf{R}_{\text{QM}})$, which, as noted, depends on multiple electronic density matrices and hence *is not derived from a single particle formalism*. It is critical to emphasize that the states $\{\mathbf{P}_I\}$ in eq 4 are *not adiabatic* but are, in fact, a basis about which the adiabatic state is instantaneously represented, as discussed in Appendix A.

It is possible to write down Euler–Lagrange equations of motion resulting from eq 4 for both $\mathbf{R}_C$ and $\{\mathbf{P}_I\}$. The

propagation for the classical nuclear degrees of freedom, $\mathbf{R}_C$, is based on the velocity Verlet[86] scheme arising from these Euler−Lagrange equations.

With respect to the propagation of $\mathbf{P}_I$, there are two variants available that are described below in algorithmic form:

- *Diabatic Algorithm 1*: If the extended Lagrangian in eq 4 is directly used to compute the time-dependent diabatic states, the Euler−Lagrange equations derived from eq 4 propagate $\mathbf{P}_I$, $\mathbf{W}_I$ in a fashion similar to that for the classical nuclear degrees of freedom. This approach is analogous to the atom-centered density matrix propagation (ADMP)[42,82−85] equations but differs through the use of multiple single particle state functions.

- *Diabatic Algorithm 2*: A "self-consistent" approximations to the diabatic states: As noted from refs 84 and 85, Born−Oppenheimer molecular dynamics (BOMD) differs from ADMP through convergence, rather than propagation, of the density matrices. Hence, it is also possible to compute $\{\mathbf{P}_I\}$ through SCF convergence, which is the $\mu_I \rightarrow 0$ limit of the extended Lagrangian above.[85] But one must keep in mind that the diabatic states thus obtained differ from those in standard BOMD in that they only provide the local electronic properties, where the word "local" is to be interpreted with reference to the classical nuclear framework, $\mathbf{R}_C$ and the coordinate representation for the quantum dynamical degrees of freedom, R_{QM}, which is in the vicinity of the nuclear configuration $\{\mathbf{R}_C; R_{QM}^{I*}\}$. Thus, $\mathbf{P}_I \equiv \mathbf{P}_I(\mathbf{R}_C; R_{QM}^{I*})$ and *Diabatic Algorithm 2* represents a diabatic implementation of BOMD, where the word diabatic is with reference to the nuclear subspace $\mathbf{R}_{QM}$.

In ref 14, it has been shown that *Diabatic Algorithm 2* above leads to an accurate set of trajectories, with minimal loss in computational efficiency with respect to *Diabatic Algorithm 1*. Hence *Diabatic Algorithm 2* is used in the current publication.

Once the diabatic state density matrices, $\{\mathbf{P}_I\}$, are computed at each time-step, the corresponding diabatic wave functions, $\{\Phi_I^{(\text{diab})}\}$, are used within a nonorthogonal CI formalism to compute the quantity, $E(\mathbf{R}_C, \{\mathbf{P}_I\}, \mathbf{R}_{QM})$, that is, the adiabatic potential surface, and gradients with respect to the classical nuclear coordinates. The critical features of the method are as follows: (a) A singular value decomposition of the single particle overlap in eq 3 yields the so-called "corresponding orbitals".[87−89] This simplifies calculation of the nonorthogonal CI Hamiltonian matrix elements. (b) The algorithm is further simplified through introduction of a combination of atom-centered and grid-centered basis functions, as outlined in Appendix B2. The quantum nuclear coordinate dependence of the electronic structure basis is eliminated through introduction of an adaptive set of grid-localized Gaussian basis functions that replace the atom-centered functions situated on the quantum nuclear degrees of freedom. These functions adapt to the position of the classical nuclear degrees of freedom. Because these functions are spread over the quantum nuclear grid, they span the electronic basis space as well and this aspect has been gauged in ref 16. The introduction of these functions allows the reuse of two-electron integrals when the CI Hamiltonian is recomputed at subsequent grid points and greatly reduces the computational effort.

In the above discussion, we have not distinguished between the cases where the entire family of diabatic Slater determinants $\{|\Phi_I^{(\text{diab})}\rangle\}$ constructed from the density matrices, $\{\mathbf{P}_I\}$, is a totally nonorthogonal set or if this set is composed of sub-

nonorthogonal sets such as $\{..., \{|^{(\text{diab})}\Phi_{i_{M-1}}^{M-1}\rangle\}, \{|^{(\text{diab})}\Phi_{i_M}^{M}\rangle\}, ...\}$, where each subset $\{|^{(\text{diab})}\Phi_{i_M}^{M}\rangle\}$ is internally orthogonal. This would, for example, be the case when a set of reference determinants, $\{..., \{|^{(\text{diab})}\Phi_{i_{M-1}=0}^{M-1}\rangle, |^{(\text{diab})}\Phi_{i_M=0}^{M}\rangle, ...\}$, are excited to produce the configurations $\{..., \{|^{(\text{diab})}\Phi_{i_{M-1}\neq 0}^{M-1}\rangle\}, \{|^{(\text{diab})}\Phi_{i_M\neq 0}^{M}\rangle\}, ...\}$, as is done in multireference CI calculations.[68] Although this distinction is not present in our theoretical development above, the numerical implementation does not include the presence of excited state determinants and hence for all test cases provided, $\{|\Phi_I^{(\text{diab})}\rangle\}$ are indeed nonorthogonal, barring uncertainties arising from numerical precision. Numerical treatments including a complete multireference study will be considered in future publications.

B. The Algorithm. Using the initial structure, the quantum nuclear grid is parametrized and an initial guess for quantum nuclear wavepacket is determined. The major components of the MC-QWAIMD approach are discussed below. The computational bottlenecks are noted in Figure 2. The adiabatic-QWAIMD approach is discussed following MC-QWAIMD.
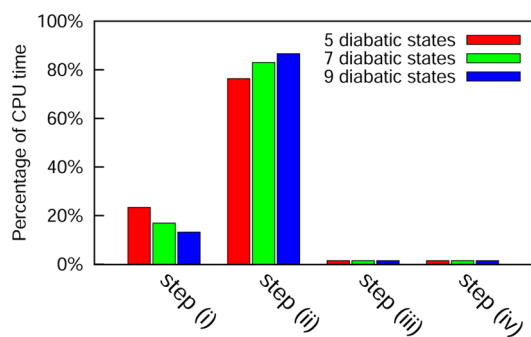

Figure 2. Fraction of CPU time spent in each portion of the MC-QWAIMD algorithm. See section IIB and Figure 3 for a detailed description of the various steps. Also see Figure 4 for computational complexity with dimensionality and system size. The CPU times here are obtained from the calculations described in the results section. Parallelization greatly reduces the overhead in steps i and ii as shown in Figure 4.

- **Step i**: Computing diabatic density matrices and associated diabatic surfaces:

(a) **Step i(a)**: At the initial time-step of dynamics, the positions $\{R_{QM}^{I*}; \mathbf{R}_C\}$ are to be obtained on the basis of the Shannon entropy sampling function. (See Appendix B1.) This leads to the diabatic states $\mathbf{P}_I(\mathbf{R}_C; R_{QM}^{I*})$ through SCF calculations at nuclear geometries, $\{R_{QM}^{I*}; \mathbf{R}_C\}$. See top-right panel of Figure 3 for an illustration of this step.

(b) **Step i(b)**: At later dynamics steps, the diabatic states are obtained either through propagation (*Diabatic Algorithm 1*) or through SCF convergence at the time-dependent geometries: $\{R_{QM}^{I*}; \mathbf{R}_C(t)\}$ (*Diabatic Algorithm 2*).

(c) **Step i(c)**: Using the $\{\Phi_I^{(\text{diab})}\}$ computed in steps i(a) and i(b), we obtain the diagonal elements for the nonorthogonal CI matrix and gradients for all quantum nuclear grid points. First, a (small) fraction of grid points is chosen using a variant of the TDDS algorithm,[4,12,16] with measure function:
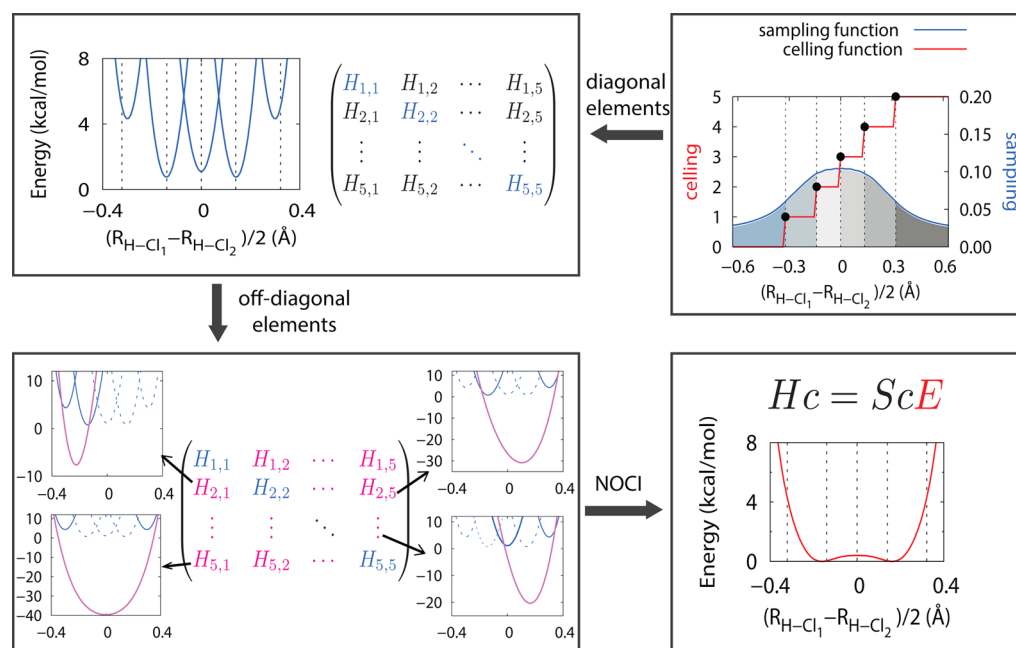
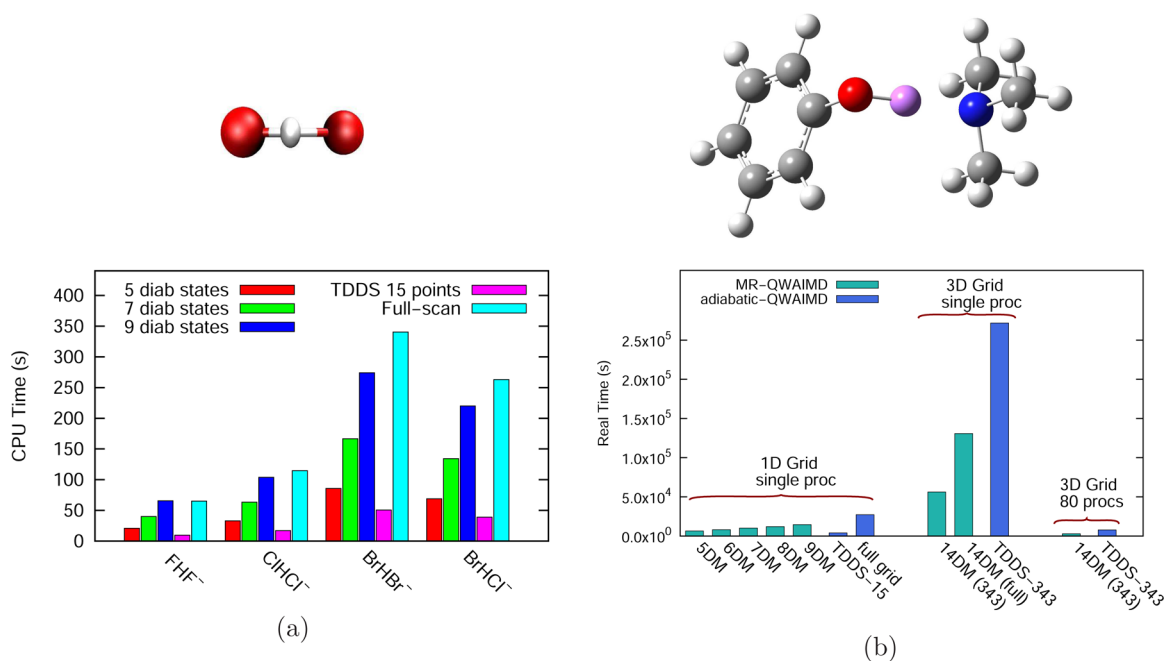**Figure 3.** The algorithm. See section IIB for details.

(a)

(b)

Figure 4. Computational complexity for potential energy and gradient calculations during each QWAIMD step. (a) All calculations include a one-dimensional treatment of the quantized proton in ClHCl$^-$. For MC-QWAIMD, data for 5, 7, and 9 diabatic states are presented, whereas for adiabatic-QWAIMD, 15 TDDS points as well as the full grid calculation are shown. (b) One-dimensional and three-dimensional treatment for the phenol−amine system. The quantized proton is shown in magenta. For three-dimensional simulations, the numbers in parentheses are the number of TDDS points where the CI matrix is computed. See eqs 5 and 6. Clearly, parallelism and TDDS greatly reduce the complexity of the problem. (For reference, on the shown scale, the full-grid calculation in three-dimensions, for adiabatic-QWAIMD, is 10^8 CPU units.)

$$\omega_{i,i}(R_{QM}) \propto \frac{\tilde{S}[\rho(R_{QM})] + 1}{\tilde{H}_{i,i} + 1} \qquad (5)$$

Here, the local Shannon entropy function of the nuclear wavepacket, $S[\rho(R_{QM})] \equiv -\rho \log(\rho)$, is a function of the wavepacket density: $\rho(R_{QM}) \equiv \chi^*(R_{QM}) \chi(R_{QM})$. Similarly, $\{H_{i,i}\}$ are the diagonal elements of the nonorthogonal CI matrix. Furthermore, $\tilde{S}$ and $\tilde{H}_{i,i}$ are

normalized to have values in $[0, 1]$, so as to have similar contributions toward the overall sampling function. The unit shifts in the numerator and denominator of eq 5 retain numerical stability. This portion of the algorithm is critical in multiple dimensions, because TDDS reduces the number of calculations required by several orders of magnitude.[4] Once the diagonal elements of the CI matrix, and its gradients, are obtained over the fraction of grid points determined using TDDS, an interpolation is

Table 2. Quantum Nuclear Grid and Mesh-Guided Basis Details

	one-dimensional representation of the quantized hydrogen		three-dimensional representation of the quantized hydrogen	
quantum nuclear grid parameters	grid size = 1.4 Å[b]	$N_{grid}{}^{a}$ = 101	grid size = 1.4 Å × 0.8 Å × 0.8 Å[c]	$N_{grid}{}^{a}$ = 97 × 49 × 49
adaptive electronic, (STO-3G) mesh	mesh size = 2 Å	$N_{basis}{}^{d}$ = 11	mesh size[e] = 1.6 Å × 0.4 Å × 0.4 Å[c]	$N_{basis}{}^{d}$ = 33

[a]Number of quantum nuclear grid points. [b]Grid oriented along the donor–acceptor axis. [c]The leading dimension is oriented along the donor–acceptor axis. [d]Number of basis functions. [e]The basis set mesh contains two parts: The inner portion of the mesh, close to the classical optimized structure, contains basis functions localized on a cubic lattice. The grid spacing for this lattice is 0.2 Å in all three dimensions and includes 27 basis functions. There is a further set of six Gaussian basis functions placed along the donor–acceptor axes, three on either side of the aforementioned cubic lattice.

constructed to obtain the same over the entire quantum nuclear grid. This yields the diabatic state surfaces and is illustrated through the top-left panel of Figure 3.

●**Step ii:** The off-diagonal elements of the nonorthogonal CI matrix are computed using transition density matrices,[14,90,91] obtained using orbital coefficients (eqs 19 and 20 in ref 14). Here again, a TDDS measure function is used to compress the quantum nuclear grid regions where these calculations are to be performed according to

$$\omega_{i,j}(R_{QM}) \propto \frac{\tilde{S}[\rho(R_{QM})] + 1}{\tilde{H}_{i,j} + 1} \qquad (6)$$

The $\{H_{i,j}\}$ are the off-diagonal elements of the CI matrix, and again $\tilde{H}_{ij}$ are bounded by unity. As in step i(c), once the off-diagonal elements of the NOCI matrix, and gradients, are obtained over the TDDS points, an interpolation is conducted to obtain the same over the entire quantum nuclear grid. At the end of this step, we have the CI matrix elements and gradients of the individual CI Hamiltonian matrix elements at every quantum nuclear grid point. (See bottom left panel of Figure 3.) Figure 4b demonstrates the power of this sampling algorithm. As the dimensionality of the quantum nuclear problem increases, TDDS and parallelism are both critical with respect to algorithmic efficiency.

●**Step iii:** The next step is to perform the nonorthogonal CI calculation. This step provides the adiabatic surface for quantum dynamics. (See bottom right panel of Figure 3.) This calculation is currently performed at every individual grid point, in parallel. However, a sampling approach here should further reduce the computational overhead when a larger number of quantum nuclear degrees of freedom are treated. These aspects will be further evaluated in future publications.

●**Step iv:** The quantum-nuclear-grid-dependent gradients obtained in steps i and ii are then used to compute gradients for classical nuclear propagation; the surface obtained in step iii leads to propagation of the quantum nuclear wavepacket.

The adiabatic-QWAIMD method differs from MC-QWAIMD in steps i–iii above. Here, the adiabatic surface is computed by locating a "special" set of nuclear configurations where the electronic structure and nuclear gradients are to be computed. This "special" set of nuclear configurations is obtained using the TDDS algorithm.[4,12,16] Following this, an interpolation procedure yields both the adiabatic surface and classical nuclear gradients,[4] leading to dynamics of the classical and quantum nuclei.

III. RESULTS AND DISCUSSION

The benchmark systems used here are the bihalide clusters: FHF⁻, ClHCl⁻, BrHBr⁻, and BrHCl⁻. We first analyze the accuracy of potential surfaces computed using diabatic states.

The R_{QM}^{I*} dependence of diabatic states is computed from the Shannon-entropy-based sampling function discussed in Appendix B1. The potential surface analysis is performed at classically optimized nuclear geometries, that is, using the gradient and Hessian optimization procedures well-known in quantum chemistry. The associated results are discussed in section IIIA. This analysis is followed by a study of QWAIMD trajectories in sections IIIB, IIIC, and IIID. All the calculations are performed using locally built modifications to a development version of the Gaussian series of electronic structure programs.

A. Adiabatic Potential Surfaces from the Diabatic State Representation. In this section we discuss the accuracy of the potential surfaces computed using the diabatic states discussed earlier. The initial structures for all the four hydrogen-bonded systems are obtained from a geometry optimization at the B3LYP/6-31+G(d,p) level of theory. For simplicity in gauging the errors introduced in MC-QWAIMD, a globally fixed Cartesian grid is employed to describe the quantum nuclear degrees of freedom. Both one-dimensional and three-dimensional grid calculations have been performed as part of our study. The potential energy surface analysis here is, however, presented along the donor–acceptor axis. The associated quantum nuclear grid parameters are given in Table 2. For these cases, a comparison of results obtained from the chosen grid size and those from a larger grid yield consistent results. For the potential energy surface calculations, the diabatic electronic structure, or the reference states, are obtained at the Hartree–Fock and DFT levels. These diabatic functions are then used within our multireference treatment presented here. The electronic basis functions include, a set of 6-31+G(d,p) Gaussian basis functions localized on the classical atoms and 11 or 33 STO-3G Gaussian basis functions distributed uniformly along the quantum nuclear grid as noted in Table 2. At the starting geometry, the grid-based basis functions are placed symmetrically and equally spaced, with reference to the quantum nuclear grid, with a grid spacing of 0.2 Å. This basis-set spacing reduces linear dependency as seen in ref 16. This choice has also been shown to have accuracy comparable to that of atom-centered aug-cc-pVTZ basis functions. (See Table 2 in ref 16.) The grid-based basis function positions adapt relative to the donor and acceptor atomic positions, as discussed in Appendix B2. Specifically, the locations of the basis functions expand and contract along with donor–acceptor distance.

In this subsection, we evaluate the use of diabatic states within the NOCI algorithm toward computing the adiabatic potential surface. In Figures 5 and 6, we provide an illustration of the potential surfaces constructed from the NOCI algorithm at equilibrium geometries obtained from gradient minimization. These are constructed using the diabatic states for the chosen set of bihalide systems where the quantum nuclear dependence of the diabatic states, that is the positions, R_{QM}^{I*}, are determined as outlined in Appendix B1. The Shannon-entropy-based sampling function described in Appendix B1 provides a higher weight at

the classically allowed, low potential regions, as well as near the classical turning points regions that are critical for quantum nuclear effects.[14,16] To further improve the sampling at the truly high potential regions as well, two diabatic states are placed at the edge of the grid. The NOCI potential surfaces are in good agreement with adiabatic surfaces obtained from scanning the quantum mechanical degrees of freedom for these set of geometries. (Also see Figure 1 which depicts the overlap between the diabatic states. The chosen states are linearly independent and help expand the size of the n-particle Hilbert space.)
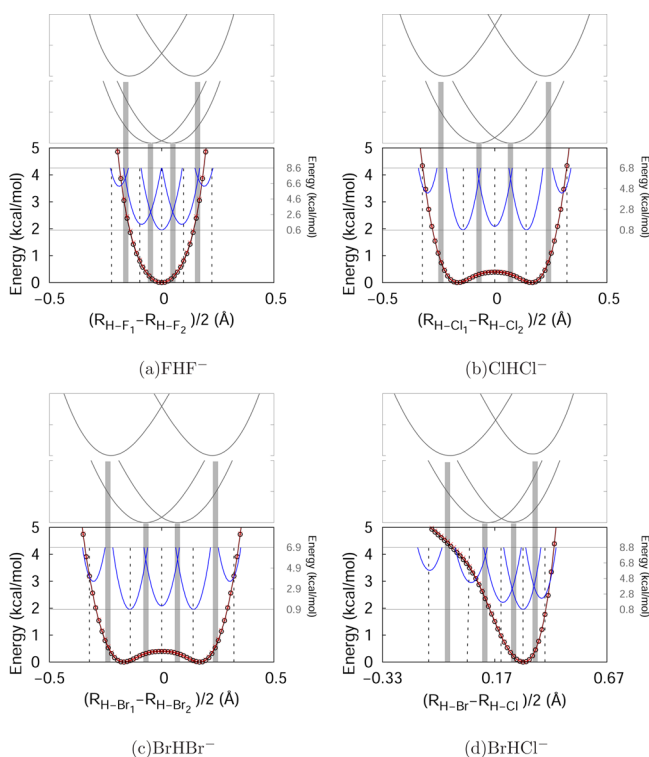

(a)FHF⁻ (b)ClHCl⁻

(c)BrHBr⁻ (d)BrHCl⁻

Figure 5. Accuracy of the adiabatic potential and mechanism of computing the adiabatic potential using multiple diabatic states. The reference states in this case are from Hartree−Fock, whereas those for Figure 6 are from DFT/B3LYP. The five central diabatic surfaces are shown in blue (energy axis on the right), and the resultant NOCI surfaces are shown in red (energy axis on left) and are in good agreement with the scanned surface shown in black. The first sets of off-diagonal CI elements are shown in the top panel. The vertical dashed lines indicate the position of diabatic states. For (d), bromine is on the left.

In Table 3, errors are computed in comparison with the adiabatic surfaces using

$$\Delta V_\eta = \sqrt{\frac{\int dx \left[(V_{\mathrm{NOCI}}(x) - V_{\mathrm{NOCI}}^{\min}) - (V_{\mathrm{adiab}}(x) - V_{\mathrm{adiab}}^{\min}) \right]^2 \eta(x)}{\int dx \, \eta(x)}}$$

(7)

Here, $V_{\mathrm{NOCI}}(x)$ is obtained using the on-the-fly nonorthogonal CI approach for determining the surface in QWAIMD, and $V_{\mathrm{adiab}}(x)$ is a ground state adiabatic potential surface obtained using a nuclear position scan. In addition, $V_{\mathrm{NOCI}}^{\min}$ and $V_{\mathrm{adiab}}^{\min}$ are the minimum values on the grid for $V_{\mathrm{NOCI}}(x)$ and $V_{\mathrm{adiab}}(x)$, respectively. Thus, $(V_{\mathrm{NOCI}}(x) - V_{\mathrm{NOCI}}^{\min})$ and $(V_{\mathrm{adiab}}(x) - V_{\mathrm{adiab}}^{\min})$ are shifted potentials that are used to gauge the relative error.

To analyze the accuracy of the potential surfaces, various choices of η were considered:

(a) A choice of $\eta_1(x) = 1$ maintains equal importance at all grid points and is used to gauge the full grid potential error.

(b) To gauge the error closer to the center of the grid where the quantum nuclear wavepacket may be expected to be localized, $\eta_2(x)$ is a step function chosen to be equal to 1 near the center of the grid (0.84 Å in spread) and zero outside this region.

(c) Because Gaussian wavepackets and ground states obtained from the potential are commonly chosen initial wavepackets, we have two additional forms for this weighting function. The function $\eta_3(x)$ is a Gaussian symmetrically centered on the grid, with the exponent chosen such that the weighting function has a value of 10^{-3} at the edges of the grid.

(d) $\eta_4(x)$ is chosen to be the ground state wavepacket density for V_{adiab}.

As shown in Table 3, the surfaces constructed from 7 and 9 diabatic states reproduce the relative potential with high accuracy.

B. MC-QWAIMD Simulation Details. The initial wavepackets for the QWAIMD simulations are chosen as ground states obtained by diagonalization of the quantum nuclear Hamiltonian in the coordinate representation. Here, the potential surface is obtained on-the-fly using the NOCI algorithm demonstrated in the previous section, whereas the kinetic energy operator is represented using "distributed approximating functionals" (DAF).[10,11,92,93]

All simulations use a 0.25 fs time step for classical nuclear propagation, and 0.05 fs time step for quantum nuclear propagation. Fifteen TDDS points are used in all adiabatic QWAIMD simulations to construct the potential surface. A number of trajectories with a varying number of diabatic states have been examined in our study in an effort to gauge the accuracy of MC-QWAIMD. The choice of initial diabatic state positions is crucial in MC-QWAIMD and we use the Shannon-entropy-based sampling functions in eq B1 to locate regions of diverse electronic structure along the quantum grid as explained in Section B1.

Energy conservation properties for all simulations are provided in Table 4. These parameters are well within the acceptable (subkcal/mol) range as compared to our previous AIMD[94−102] and QWAIMD[4,14,15] studies. The computational scaling of the algorithm is compared with a-QWAIMD in Figure 4.

C. Structural, Dynamical, and Vibrational Properties Obtained from the MC-QWAIMD Simulations. In this section, we will examine the structural and dynamical properties of the benchmark systems as obtained from MC-QWAIMD trajectories. A large number of simulations have been performed for the four bihalide hydrogen-bonded systems. The initial nuclear geometries, quantum nuclear grid definitions, grid-based electronic basis function positions, levels of theory, and initial wavepacket definitions are as stated in sections IIIA and IIIB. In addition, the average values for the classical nuclear and quantum nuclear kinetic energies are listed in Table 5. In each case the length of simulation is 2 ps. As may be noted from Table 5, the average or equilibrated quantum nuclear and classical nuclear kinetic energies per degree of freedom are very different for all systems. This is critical because equilibration between these disparate subsystems is not desirable on account of the expected zero point energy for the quantum nuclear degrees of freedom. As noted from Figure 7, the kinetic energies for the quantum and
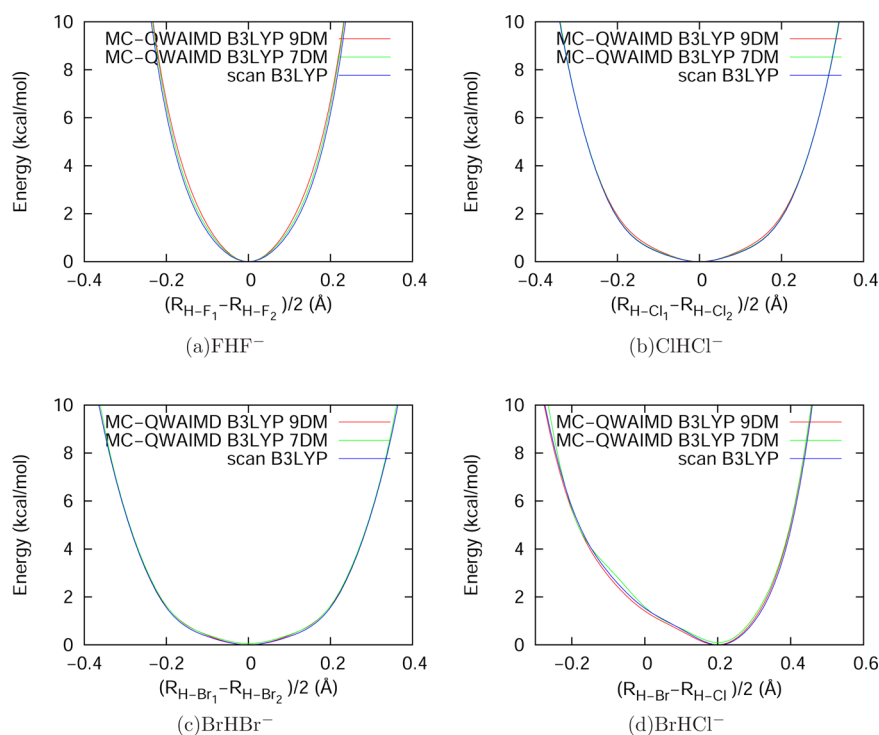
Figure 6. Adiabatic potentials computed at the B3LYP level using the MC-QWAIMD formalism.

Table 3. Error in the Potential Surface Computed at the Optimized Geometries[a]

| | | MC-QWAIMD[b] | | | | | | a-QWAIMD[c] | |
| | | HF | B3LYP | HF | B3LYP | HF | B3LYP | HF | HF |
		(5)[d]	(5)[e]	(7)[d]	(7)[e]	(9)[d]	(9)[e]	9[f]	15[f]
FHF⁻	η_1	11.183	13.569	4.063	5.404	1.947	1.744	1.343	0.181
	η_2	5.260	5.644	0.222	0.505	0.050	0.447	0.246	0.020
	η_3	7.857	9.232	2.261	2.974	1.007	0.943	0.648	0.080
	η_4	0.281	0.638	0.013	0.139	0.032	0.145	0.133	0.009
ClHCl⁻	η_1	5.964	7.409	2.060	2.249	0.976	0.390	0.100	0.035
	η_2	3.270	3.849	0.183	0.133	0.018	0.043	0.053	0.007
	η_3	4.381	5.354	1.190	1.258	0.513	0.199	0.066	0.014
	η_4	0.520	0.629	0.040	0.033	0.017	0.026	0.063	0.004
BrHBr⁻	η_1	5.234	6.497	1.755	2.063	0.735	0.331	0.118	0.040
	η_2	2.918	3.433	0.155	0.149	0.017	0.016	0.039	0.012
	η_3	3.865	4.720	1.005	1.170	0.380	0.167	0.062	0.018
	η_4	0.562	0.658	0.051	0.027	0.019	0.012	0.049	0.008
BrHCl⁻	η_1	5.395	7.569	1.320	2.197	0.374	0.613	0.313	0.174
	η_2	2.465	3.731	0.160	0.253	0.030	0.143	0.331	0.179
	η_3	3.830	5.435	0.744	1.266	0.187	0.333	0.322	0.177
	η_4	0.506	0.842	0.053	0.092	0.025	0.086	0.337	0.175

[a]The quantities shown are the values of Δ_η from eq 7 for different choices of η. The units for ΔV_η are in kcal/mol. [b]Multiconfigurational QWAIMD. [c]Adiabatic QWAIMD using TDDS. [d]The reference states are computed at the Hartree−Fock level of theory. The numbers in parentheses are the number of diabatic states. [e]The reference states are computed at the DFT/B3LYP level of theory. The numbers in parentheses are the number of diabatic states. [f]Number of TDDS points used in a-QWAIMD.

classical degrees of freedom remain well separated. However, the heavier systems do display classical kinetic energies with greater magnitudes and larger spreads. Instantaneous diagonalization of the quantized nuclear degree of freedom indicates that the quantum wavepacket remains mostly on the ground eigenstate, with minor excited state contribution for BrHCl⁻.

As part of the structural analysis we also present the radial distribution function for the donor−acceptor distance in Figure 8; the corresponding quantum wavepacket and potential energy

surface evolution for nine diabatic states are in Figure 9 and Figure 10. An average shared proton distribution is provided on the top panels in Figure 9. As noted in Figure 8, there is a significant dependence of the donor−acceptor distance on the classical temperature. Compare Figure 8 with Table 5. As expected, this is true to a greater extent for the lighter (FHF⁻ and ClHCl⁻) systems than for the heavier nuclear systems (BrHBr⁻ and BrHCl⁻) where a similar change in temperature has little effect on the donor−acceptor distance distribution. In all cases

Table 4. Energy Conservation Properties for the QWAIMD Trajectories[a]

	FHF⁻	ClHCl⁻	BrHBr⁻	BrHCl⁻
MC-QWAIMD 5 diabatic states	0.249	0.057	0.114	0.193
MC-QWAIMD 7 diabatic states	0.355	0.059	0.098	0.190
MC-QWAIMD 9 diabatic states	0.392	0.060	0.091	0.190
adiabatic-QWAIMD with 15 TDDS points	0.056	0.028	0.060	0.156

[a]The quantities shown are the standard deviation in total energy during the trajectory. Units are in kcal/mol, and all simulations are 2 ps long.

the average values shown in the figure are about a hundredth of an angstrom away from the respective experimental values also noted in Figure 8. The location of the classical turning-point in each case can be determined from the spike at the edge of the distribution function, because the donor and acceptor atoms are treated using classical dynamics. In Figures 9 and 10, the quantum wavepacket motion is shown to be coupled with the potential surface generated by the classical nuclei. As we will see in the next section, the oscillation frequency of the wavepacket contours roughly coincides with the donor−acceptor stretch frequency. For the symmetric systems (FHF⁻, ClHCl⁻, and BrHBr⁻), the breathing frequency of the donor−acceptor oscillations is evident from the changes in wavepacket amplitude at the central grid point (through the frequency of appearance of the red-contour). However, the wavepacket appears totally symmetric in these cases, which effectively retains the wavepacket centroid at the central grid point all through the dynamics. Thus, the effect of donor−acceptor oscillation is not captured in the dynamics of the centroid, although it is present in the wavepacket evolution for the symmetric FHF⁻, ClHCl⁻, and BrHBr⁻ systems. This symmetric behavior is obviously absent in the case of BrHCl⁻. As a result, the wavepacket centroid is expected to follow closely to the green contour in Figure 9d and the dynamics of the centroid, in this case, does capture, to some extent, the effect of donor−acceptor oscillations. These effects due to symmetry are also confirmed upon inspection of Figure 10. The average wavepacket density on the top panels in Figure 9 indicates the extent of delocalization of the hydrogen nuclear wave function in each case. The greater spread of the wavepacket for ClHCl⁻ is due to the presence of quartic and sixth-order terms in the potential as already noted in ref 4.

D. Vibrational Analysis from MC-QWAIMD Trajectories Constructed Using the Unified Velocity/Flux Autocorrelation Function.

The vibrational density of states are obtained through the Fourier transform of a unified velocity/flux autocorrelation function, with data computed using the MC-QWAIMD trajectories. Here, the wavepacket flux and the classical nuclear velocities are combined as follows:

$$I_{\mathbf{V},\mathbf{J}} = \lim_{T\to\infty} \int_{t=0}^{t=T} dt \; e^{-i\omega t}\{\langle \mathbf{V}(0)\cdot\mathbf{V}(t)\rangle_{\mathrm{C}} + \langle \mathbf{J}(0)\cdot\mathbf{J}(t)\rangle_{\mathrm{Q}}\} \tag{8}$$

where the expectation value of wavepacket flux is $J(t) = \mathcal{R}[\langle\psi(t)|(-i\hbar/m)\nabla|\psi(t)\rangle]$. Here, $\mathcal{R}[\cdots]$ represents the real part of the complex number in square brackets. The symbols $\langle\cdots\rangle_{\mathrm{C}}$ and $\langle\cdots\rangle_{\mathrm{Q}}$ represent classical and quantum ensemble average. That is the ensemble average is constructed from the classical and quantum dynamical portions of the trajectory. The quantity $\mathbf{V}$ is the $3N$-dimensional nuclear velocity vector and ω is the frequency. The two ensemble averages $\langle\mathbf{V}(0)\cdot\mathbf{V}(t)\rangle_{\mathrm{C}}$ and $\langle\mathbf{J}(0)\cdot\mathbf{J}(t)\rangle_{\mathrm{Q}}$ are calculated using convolution theorem[103] in the following manner:

$$\lim_{T\to\infty} \int_{t=0}^{t=T} dt \; e^{-i\omega t}\langle\mathbf{X}(0)\,\mathbf{X}(t)\rangle$$
$$= \lim_{T\to\infty} \sum_{i=1}^{N}\sum_{j=1}^{3} \int_{t=0}^{t=T} dt \; e^{-i\omega t} \int_{t'=0}^{t'=T} dt' \; X_{i,j}(t')\,X_{i,j}(t'+t)$$
$$= \lim_{T\to\infty} \sum_{i=1}^{N}\sum_{j=1}^{3} \left|\int_{t=0}^{t=T} dt \; e^{-i\omega t} X_{i,j}(t)\right|^2 \tag{9}$$

Equation 8 is to be contrasted with correlation functions used in refs 104−107 to compute vibrational spectra from quantum-classical trajectories. In contrast with expressions used in refs 104 and 105, the flux expression in eq 8 is computed from quantum dynamics and hence may include contributions from more than one excited state depending upon the temperature of the simulation. Second, the classical degrees of freedom are, in general, anharmonic, because the dynamics here is computed using the potentials extracted from electronic structure calculations. Finally, the expression in eq 8 includes the velocity autocorrelation function and the flux autocorrelation function. Because the latter is the quantum-mechanical analogue of velocity, eq 8 represents a vibrational density of states. Infrared intensities can also be included by directly computing the time-dependent, wavepacket averaged dipoles, but these are not considered in this publication.

The results here are presented for 5, 7, and 9 diabatic states. These results are compared with gas-phase spectroscopy experiments,[43,49−58] with results obtained from other theories that include quantum-nuclear treatment,[5,45,46,48,59] and with the TDDS implementation of adiabatic QWAIMD using 15 TDDS points. In addition to the vibrational fundamentals here, the dynamics results also provide combination bands such as those obtained through a mixture of the donor−acceptor motion with wavepacket motion. However, our treatment here is one-dimensional for the quantum wavepacket, and hence we only probe the asymmetric proton stretch, ν_3, and the symmetric donor−acceptor stretch, ν_1. The vibrational fundamentals

Table 5. MC-QWAIMD Average Nuclear Kinetic Energies (kcal/mol)

	FHF⁻		ClHCl⁻		BrHBr⁻		BrHCl⁻	
	K_{C}[a]	K_{Q}[b]	K_{C}[a]	K_{Q}[b]	K_{C}[a]	K_{Q}[b]	K_{C}[a]	K_{Q}[b]
5[c]	0.331 76	1.094 75	0.083 40	0.690 20	2.676 77	1.149 28	0.668 55	1.463 92
7[c]	0.365 65	1.038 97	0.097 89	0.577 31	2.624 31	1.090 36	0.700 18	1.389 43
9[c]	0.382 22	1.029 37	0.098 71	0.569 40	2.610 13	1.085 97	0.700 43	1.373 81
15[d]	0.188 76	1.122 36	0.128 45	0.562 12	2.547 94	1.084 78	0.625 69	1.141 57

[a]Average nuclear kinetic energy for the classical nuclear subsystem. [b]Average nuclear kinetic energy for the quantum nuclear subsystem. [c]Number of diabatic states in MC-QWAIMD. [d]This quantity is the number of TDDS points for the adiabatic,TDDS-based QWAIMD.
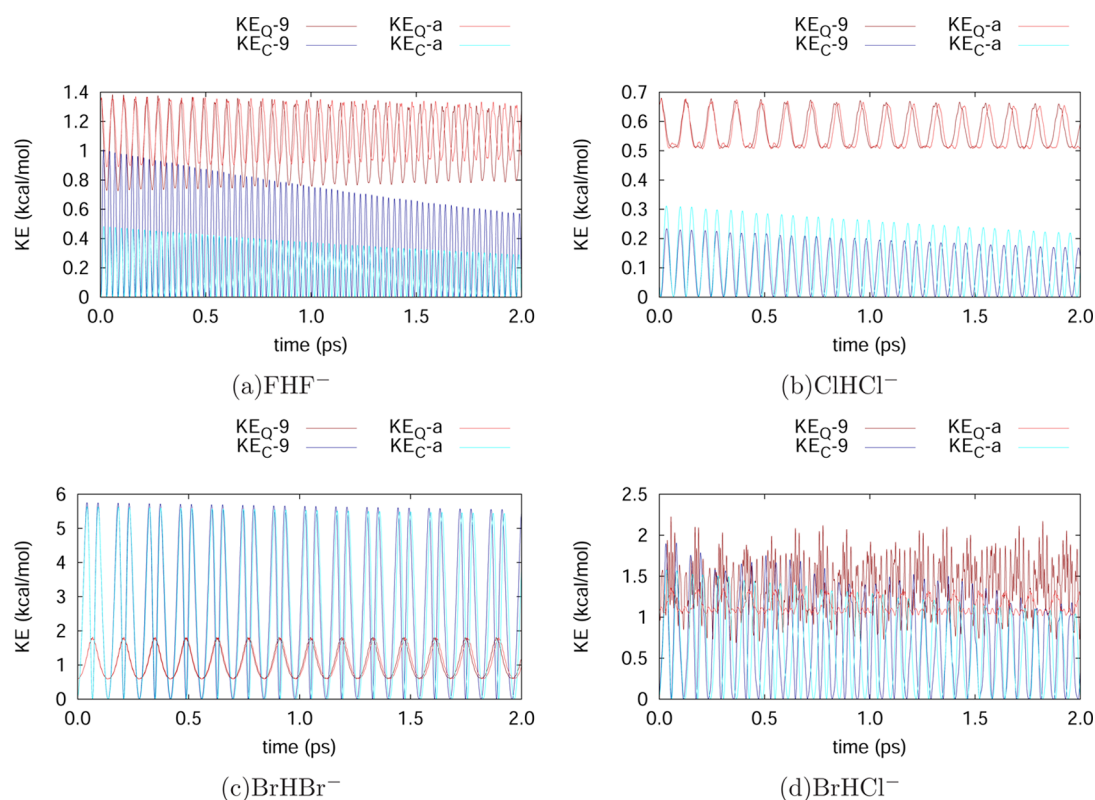
Figure 7. Time evolution of the classical (KE_C; dark blue and light blue) and quantum (KE_Q; dark red and light red) nuclear kinetic energies for FHF^- (a), $ClHCl^-$ (b), $BrHBr^-$ (c), and $BrHCl^-$ (d). In each figure the vertical axis depicts the kinetic energy in kcal/mol. The KE-9 refers to 9 diabatic states in MC-QWAIMD, and KE-a refers to adiabatic-QWAIMD. As noted, the kinetic energies for the quantum and classical degrees of freedom remain well separated.
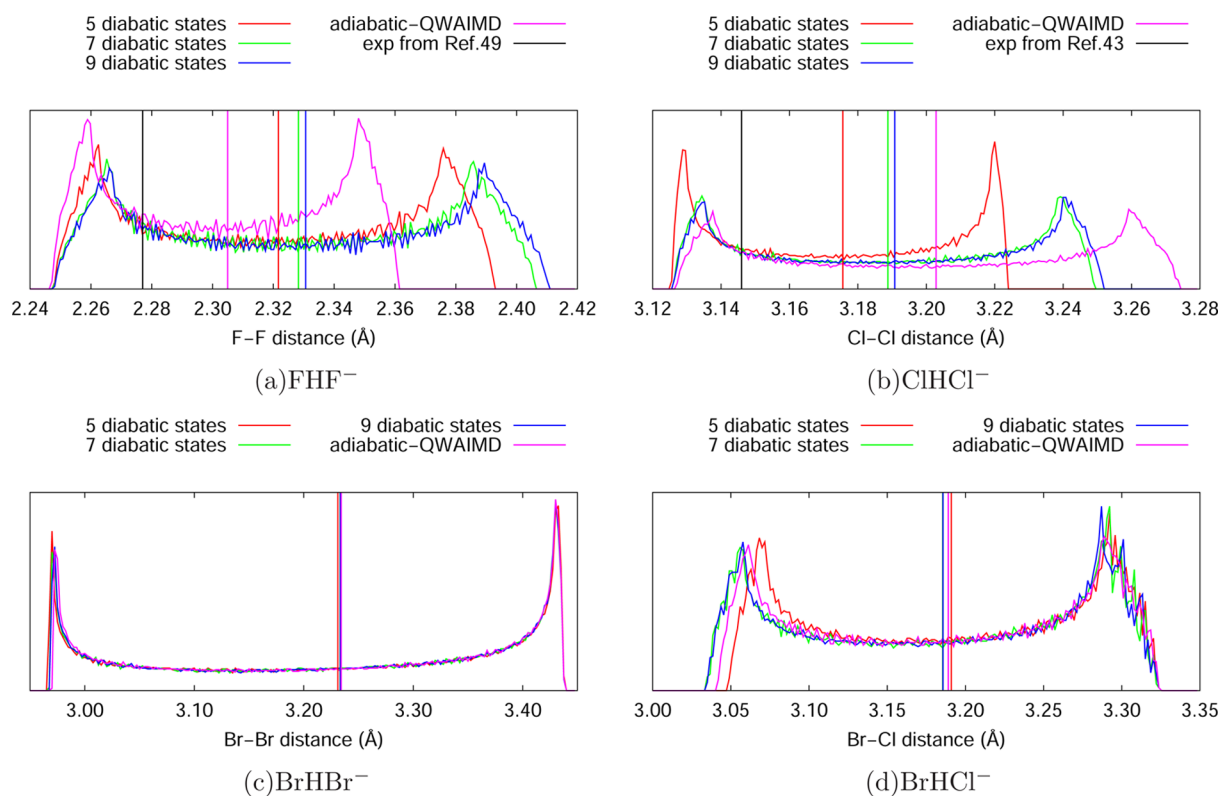

Figure 8. Donor−acceptor radial distribution function for FHF^- (a), $ClHCl^-$ (b), $BrHBr^-$ (c), and $BrHCl^-$ (d). Each figure contains results from MC-QWAIMD using 5 (red), 7 (green), and 9 (blue) diabatic states as well as adiabatic, TDDS-based QWAIMD with 15 TDDS points (magenta). Experimental value are also quoted, where available.
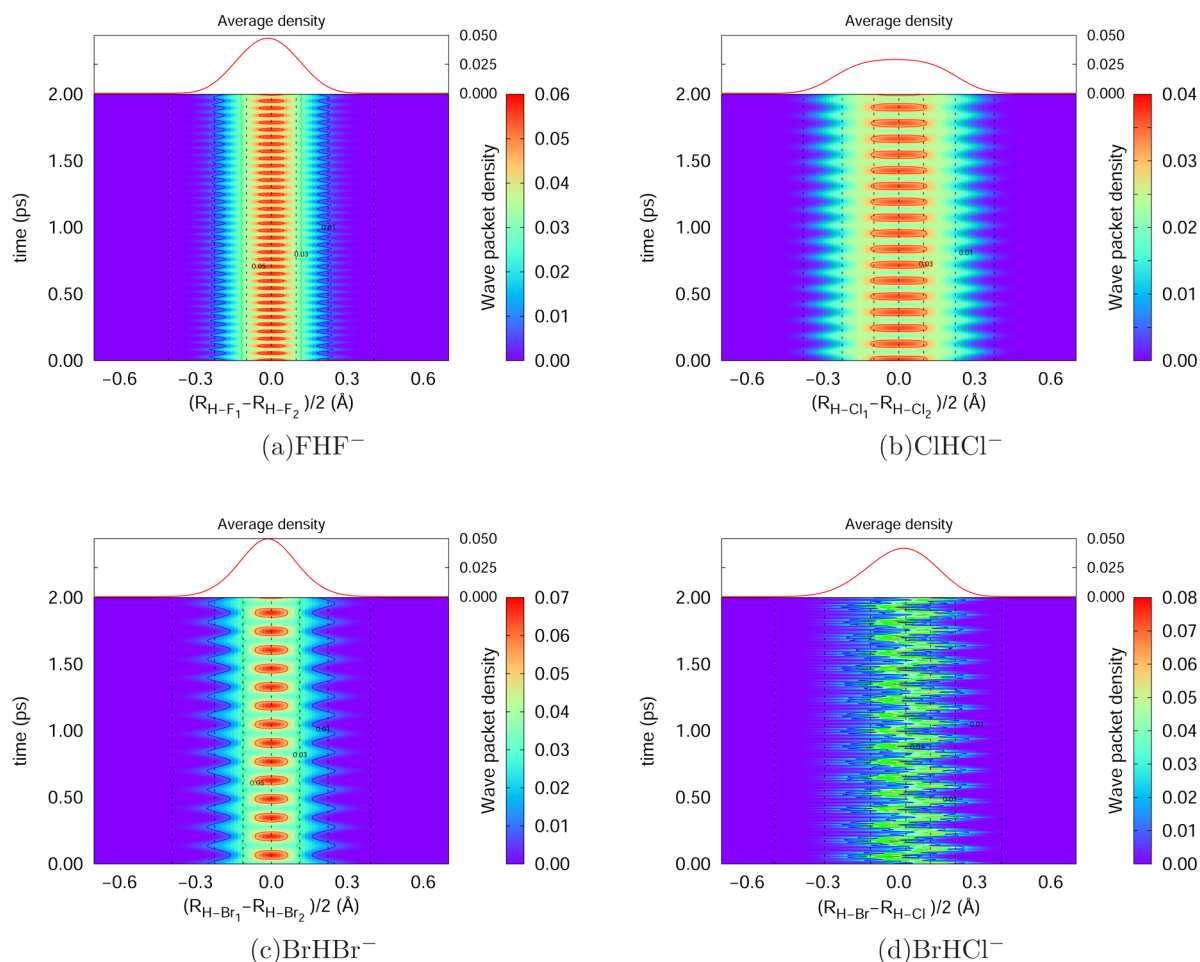
2274

dx.doi.org/10.1021/ct5002347 | *J. Chem. Theory Comput.* 2014, 10, 2265−2280

Figure 9. Quantum wavepacket density evolution for quantized proton in the MC-QWAIMD simulation using 9 diabatic states. The black dotted lines indicate the positions, R_{QM}^{1*}, of the diabatic states. The position of the two outermost diabatic states coincide with the edge of the quantum nuclear grid. The time-averaged wavepacket density is shown on the top panel within each figure.

obtained from the Fourier transform of velocity/flux autocorrelation functions are provided in Tables 6−9 along with comparisons to experiments. The combination bands can be noted from the wavepacket flux spectrum presented in Figure 11.

For the case of FHF⁻, as the number of diabatic states is increased, we notice a red shift in the MC-QWAIMD frequencies, which brings these in closer agreement with experiment. The red shift is to be expected because a small number of diabatic states generally results in a relatively confined potential surface to yield higher vibrational frequencies.

We also note that the best available theoretical result for ν_3 in this particular system is due to Hirata and co-workers.[59] In ref 59, the authors use a time-independent formalism that is constructed using vibrational SCF[48] in conjunction with a coupled-cluster potential. The corresponding ν_3 value is 1343 cm⁻¹. The result from MC-QWAIMD using 9 diabatic states is 45 cm⁻¹ higher than the VSCF value. This is related to the one-dimensional treatment here, because it is known from our previous adiabatic QWAIMD studies in ref 4 (also see Table 1) that increased dimensionality of the quantum system lowers the transition energy through coupling of the bending and stretching modes. It is also useful to note by comparison of Tables 1 and 6 that such coupling is expected to be lower for FHF⁻ than for ClHCl⁻. The symmetric stretch frequency ν_1 from QWAIMD (609 cm⁻¹) and MC-QWAIMD (616 cm⁻¹) are in closer agreement with VSCF (628 cm⁻¹). A comparative study that probes the role of multiple

potentials within our dynamical treatment will be considered in a future publication.

With regard to combination bands, we find a peak in the flux spectrum corresponding to $\nu_3 + \nu_1$ at about 2000 cm⁻¹. This result is about 2.5% in error with respect to the corresponding experimental value of 1849 cm⁻¹ in ref 49.

In Table 7 we provide results for ClHCl⁻. Similar to the case of FHF⁻, there is a lowering here in the ν_1 and ν_3 transition frequencies with increasing number of diabatic states. However, unlike in the case of FHF⁻, there is greater coupling between the bending and asymmetric stretch in ClHCl⁻, as already noted in ref 4. As a result, a three-dimensional QWAIMD treatment yields both the ν_3 fundamental (723 cm⁻¹) and the $\nu_1 + \nu_3$ combination band origin (970 cm⁻¹) in good agreement with experiment (978 cm⁻¹ [43]). By comparison, in the current one-dimensional calculations, the first combination band origin is found to be at ≈910 cm⁻¹.

For the case of BrHBr⁻, again the ν_3 frequencies drop as the number of diabatic states is increased. The results from simulations with a larger number of diabatic states are closer to experiment, as seen in Table 8. In Figure 11, we note the presence of a series of combination bands of the kind: $\nu_1 + n\nu_3$, for different values of n. The heavier donor/acceptor nuclear mass leads to a greater perturbation on the flux and as a result multiple combination bands are seen in the spectrum.
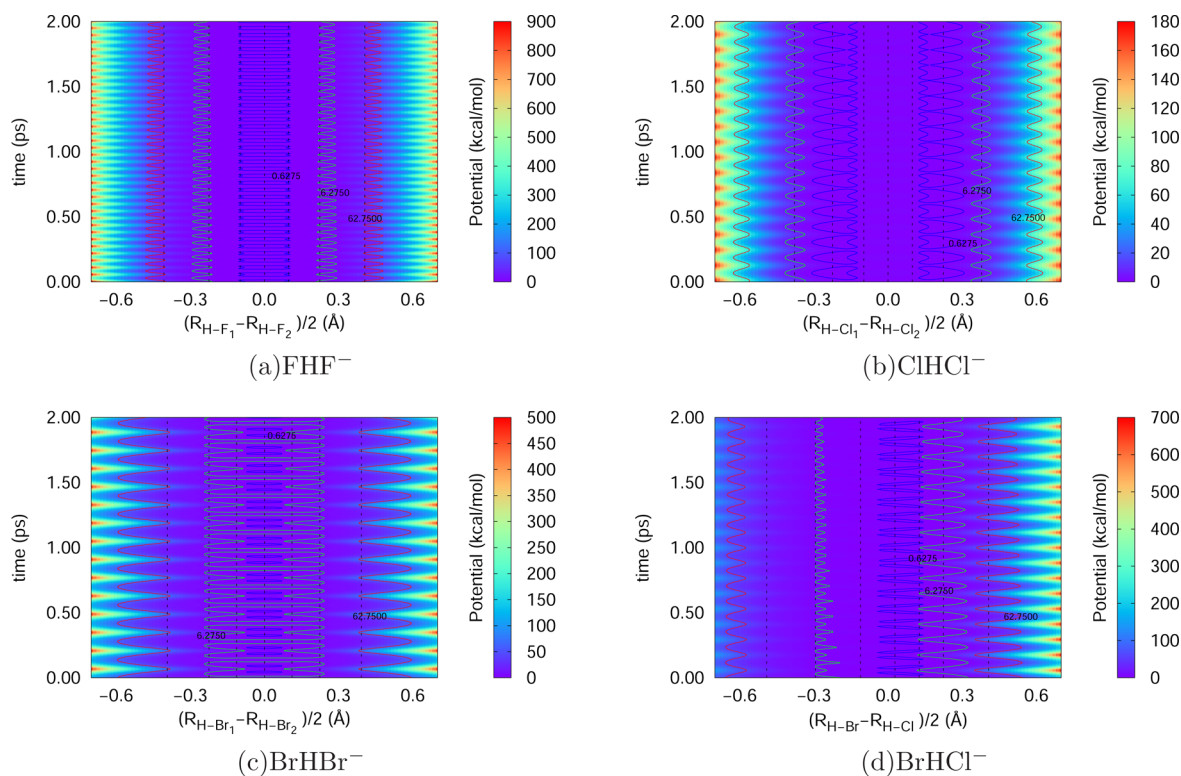
Figure 10. Potential surface evolution for quantized proton in the MC-QWAIMD simulations using 9 diabatic states. The black dotted lines indicate the position of diabatic states.

Table 6. Comparison of FHF⁻ Vibrational Fundamentals with Experiment and with Other Theories

		ν_1 (cm^{-1})	ν_3 (cm^{-1})
experiment	gas phase[49]	583	1331
	Ne matrix[50]		1379
	Ar matrix[50,51]		1377
	Ar matrix[52]		1364
harmonic	MP2/aug-cc-pVTZ	634	1306
anharmonic VSCF[a]		628	1343
anharmonic VCI[b]		580	1313
MC-QWAIMD	9 diabatic states	616	1388
	7 diabatic states	619	1400
	5 diabatic states	631	1480

[a]From ref 59, where Hirata and co-workers use a time-independent formalism that is constructed using vibrational SCF[45−48] in conjunction with a coupled-cluster potential. [b]From ref 59, where Hirata and co-workers use a time-independent formalism that is constructed using vibrational CI[45−48] in conjunction with a coupled-cluster potential.

For BrHCl⁻ again, all properties converge at 7 diabatic states; 7 diabatic states and 9 diabatic states lead to identical results. The classical velocity spectra have good agreement between the MC-QWAIMD and adiabatic-QWAIMD. The adiabatic-QWAIMD spectrum is slightly blue-shifted as compared to the MC-QWAIMD spectra.

IV. CONCLUDING REMARKS

In this paper, the multiconfigurational quantum wavepacket ab initio molecular dynamics (MC-QWAIMD) approach is used to study structural and vibrational properties for a set of bihalide, hydrogen-bonded systems. The MC-QWAIMD method has the following features: (a) The "on-the-fly" electronic structure is

Table 7. Comparison of ClHCl⁻ Vibrational Fundamentals with Experiment and with Other Theories

		ν_1 (cm^{-1})	ν_3 (cm^{-1})
experiment	gas phase[43]	318	723
	Ar matrix[53−56]		696
	Kr matrix[53]		663
	Xe matrix[53]		644
harmonic	MP2/aug-cc-pVTZ	345	648
NEO-MP2(ee+ep) [ref 5]		334	
CC-VSCF-MP2 [ref 5]		327	925
3D QWAIMD[a]	B3LYP/6-31+G*[b]	300	806
	B3LYP/6-31+G*[c]	254	723
MC-QWAIMD	9 diabatic states	282	626
	7 diabatic states	286	639
	5 diabatic states	317	800

[a]From ref 4, which also suggests that a three-dimensional treatment is essential due to greater coupling between the asymmetric stretch and bend modes. [b]Internal kinetic energy corresponding to a temperature of 323.50 K. [c]Internal kinetic energy corresponding to a temperature of 714.45 K.
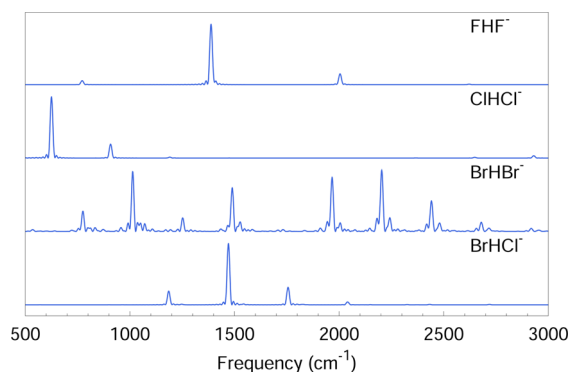
computed using a nonorthogonal configurational interaction formalism, where the individual configurations are Slater determinants that approximate diabatic states. (b) The diabatic states are propagated using an approximation based on an extended Lagrangian treatment involving multiple electronic density matrices and classically treated nuclei. (c) The diabatic approximation for these states is further strengthened by eliminating the quantum nuclear position dependence of the electronic basis. Instead, adaptive-mesh-based Gaussian electronic basis functions are introduced and these encompass the quantum nuclear grid region. This allows great simplification in computing the "on-the-fly", quantum-grid-dependent non-

Table 8. Comparison of BrHBr⁻ Vibrational Fundamentals with Experiment

		ν_1 (cm^{-1})	ν_3 (cm^{-1})
experiment	Ar matrix[57,58]	164	728
	Kr matrix[53]		687
	Xe matrix[53]		646
harmonic	MP2/aug-cc-pVTZ	210	692
MC-QWAIMD	5 diabatic states	240	855
	7 diabatic states	238	794
	9 diabatic states	238	776
adiabatic-QWAIMD	15 TDDS points	237	785

Table 9. BrHCl⁻ Vibrational Fundamentals from MC-QWAIMD and Adiabatic QWAIMD

		ν_1 (cm^{-1})	ν_3 (cm^{-1})
harmonic	MP2/aug-cc-pVTZ	185	1531
MC-QWAIMD	5 diabatic states	292	1610
	7 diabatic states	285	1498
	9 diabatic states	285	1471
adiabatic-QWAIMD	15 TDDS points	274	1462

Figure 11. Fourier transform of the flux autocorrelation function from MC-QWAIMD trajectories. All trajectories use 9 diabatic states. Combination bands of the kind $\nu_1 + n\nu_3$ caused by perturbation from heavy donor/acceptor nuclear motion are shown.

orthogonal configurational interaction formalism (with negligible loss in accuracy), where the CI-matrix elements are easily calculated through reuse of two-electron integrals as a result of the diabatic approximation. (d) At the initial time-step, the diabatic states are located using a Shannon-entropy-based sampling function that facilitates the creation of localized electronic structure groups. The sampling function depends on the nuclear wavepacket and an approximation to the potential surface.

The method is benchmarked for a series of bihalide systems: FHF⁻, ClHCl⁻, BrHBr⁻, and BrHCl⁻. First, the accuracy of Shannon-entropy-based sampling function in determining the initial diabatic state approximations and effects of using the adaptive-mesh-based Gaussian electronic basis functions are probed by computing potential surfaces for the chosen systems. The potential surfaces are found to be in good agreement with calculations that use standard atomic scan techniques. Next, structural distribution functions are computed from the MC-QWAIMD trajectories. The resultant structural features such as donor−acceptor distances are found to be in good agreement with experiments. Finally, vibrational properties are computed using the quantum wavepacket flux. The wavepacket flux allows

the direct computation of the spectral transition frequencies including both vibrational fundamentals and approximations to the combination band origins. It is found that the method provides these spectral features in reasonable agreement with experiments and other theories.

■ APPENDIX A: EVALUATION OF THE ENERGY FUNCTIONAL, $E(R_C,\{P_I\},R_{QM})$, USING "ON-THE-FLY" NONORTHOGONAL CI

The multiple density matrices are coupled through the energy function, $E(\mathbf{R}_C,\{\mathbf{P}_I\},R_{QM})$, which is obtained using nonorthogonal CI:

$$
\begin{pmatrix} H_{1,1} & \cdots & H_{1,N_{DM}} \\ \vdots & \ddots & \vdots \\ H_{N_{DM},1} & \cdots & H_{N_{DM},N_{DM}} \end{pmatrix} \begin{pmatrix} c_1^{(n)} \\ \vdots \\ c_{N_{DM}}^{(n)} \end{pmatrix}
$$
$$
= \begin{pmatrix} 1 & \cdots & S_{1,N_{DM}} \\ \vdots & \ddots & \vdots \\ S_{N_{DM},1} & \cdots & 1 \end{pmatrix} \begin{pmatrix} c_1^{(n)} \\ \vdots \\ c_{N_{DM}}^{(n)} \end{pmatrix} E(\mathbf{R}_C, \{\mathbf{P}_I\}, R_{QM})
$$
(A1)

where the electronic Hamiltonian is written in second quantized form in some orthonormal basis, $\{\chi_e^M\}$, as

$$
\hat{H} = \sum_{l,k} \langle \chi_l^M | h | \chi_k^M \rangle a_l^{M\dagger} a_k^M + \frac{1}{2} \sum_{l,k,p,q} \langle \chi_l^M \chi_k^M | \chi_p^M \chi_q^M \rangle a_l^{M\dagger} a_k^{M\dagger} a_q^M a_p^M
$$
(A2)

and the overlap is shown in eqs 2 and 3. To obtain the Hamiltonian matrix elements and the overlap matrix elements in eq A1, it is convenient to construct a singular value decomposition (SVD)[108] of s^{IJ} in eq 3:

$$
[s^{I,J}]_{k,l} = U_{k,k}\sigma_k^{I,J}[V^\dagger]_{k,l}
$$
(A3)

or

$$
[s^{I,J}] = \mathbf{U}\sigma^{I,J}\mathbf{V}^\dagger
$$
(A4)

where $\mathbf{U}$ and $\mathbf{V}$ contain the left and right singular vectors obtained from SVD of s^{IJ}, with singular values $\{\sigma_i^{I,J}\}$. These transformations yield the so-called "corresponding orbitals",[87−89]

$$
|\tilde{\chi}_i^I\rangle = \sum_k U_{ki} |\chi_k^I\rangle
$$
(A5)

$$
|\tilde{\chi}_i^J\rangle = \sum_k V_{ki} |\chi_k^J\rangle
$$
(A6)

that form a biorthogonal set according to

$$
\langle \tilde{\chi}_i^I | \tilde{\chi}_j^J \rangle = \sum_{k,l} U_{ki}^* \langle \chi_k^I | \chi_l^J \rangle V_{lj} = \sum_{k,l} U_{ki}^* [s^{I,J}]_{k,l} V_{lj}
$$
$$
= [U^\dagger s^{I,J} V]_{ij} = \sigma_i^{I,J} \delta_{i,j}
$$
(A7)

We present a few comments with respect to the corresponding orbital set, $\{\{\tilde{\chi}_i^I\}; \{\tilde{\chi}_j^J\}\}$: Because $\mathbf{U}$ and $\mathbf{V}$ are orthogonal matrices, the individual sets $\{\tilde{\chi}_i^I\}$ and $\{\tilde{\chi}_j^J\}$ are such that each transformed orbital from the set I is orthonormal with respect to the transformed orbitals in set J, as seen from eq A7. Thus, the Unitary transformations $\{\chi_i^I\} \rightarrow \{\tilde{\chi}_i^I\}$ and $\{\chi_j^J\} \rightarrow \{\tilde{\chi}_j^J\}$ orthogonalize the elements belonging to the two sets. However, because $|\Phi_I^{(diab)}\rangle$ is a Slater determinant comprising orbitals $\{\chi_i^I\}$,

the determinant remains invariant to within a phase[109] when represented in terms of the single particle functions $\{\tilde{\chi}_i^I\}$. This is similarly the case for $|\Phi_j^{(\text{diab})}\rangle$. Thus, the overlap, $\mathcal{S}_{I,J} \equiv \langle \Phi_I^{(\text{diab})} | \Phi_J^{(\text{diab})} \rangle = \text{Det}[s_{I,J}]$, is simplified in the SVD set as follows:

$$\mathcal{S}_{I,J} \equiv \langle \Phi_I^{(\text{diab})} | \Phi_J^{(\text{diab})} \rangle = \prod_i \sigma_i^{I,J} \tag{A8}$$

Similarly, the matrix elements for the nonorthogonal CI-Hamiltonian in eq A1 are given by

$$H_{I,J} = \sum_j \langle \tilde{\chi}_j^I | h | \tilde{\chi}_j^J \rangle \prod_{i \neq j} \sigma_i^{I,J} + \frac{1}{2} \sum_{i,j} \langle \tilde{\chi}_i^I \tilde{\chi}_j^I \| \tilde{\chi}_i^J \tilde{\chi}_j^J \rangle \prod_{m \neq i,j} \sigma_m^{I,J} \tag{A9}$$

These equations can be further simplified on the basis of the level of singularity of the overlap, $s^{I,J}$, or level of noncoincidence[87−89,91] of the single particle vector spaces $\{\{\tilde{\chi}_i^I\}; \{\tilde{\chi}_j^J\}\}$. This aspect is rigorously analyzed in ref 14; see section IVA.1 in ref 14 for details. The key point to note is that when the single particle vector spaces corresponding to $|\Phi_I^{(\text{diab})}\rangle$ and $|\Phi_J^{(\text{diab})}\rangle$ do not *coincide*, $s^{I,J}$ is singular and it is only the noncoincidental subspace that appears in the one- and two-particle matrix elements defined in eq A9. Once the Hamiltonian and overlap are obtained as discussed above, the generalized eigenvalue problem, eq A1, is solved to obtain the ground state that is used in the current publication. In addition, classical nuclear gradients are also obtained as discussed in section IVD, Appendix A, and Appendix B in ref 14 and used in the tests provided in the current publication.

■ APPENDIX B: COMPUTATIONAL ASPECTS

There are two critical computational aspects to the algorithm. The first part deals with the determination of R_{QM}^{I*} at time $t = 0$ and hence the valence-bond type diabatic functions with density matrices $\mathbf{P}_I(R_C; R_{\text{QM}}^{I*})$. The second aspect deals with the fact that, in contrast to conventional electronic structure approaches, the single-particle functions, $\{|\chi_i^I\rangle\}$, here are expressed using a combination of atom-centered Gaussian basis functions and a set of Gaussian basis functions the centers for which are localized on a spatial adaptive mesh.[14,16] This is important for the computational efficiency of our algorithm. These computational aspects are discussed in the subsections below.

1. Determination of $\{R_{\text{QM}}^{I*}\}$ for the Diabatic States $P_I(R_C; R_{\text{QM}}^{I*})$

The grid positions, R_{QM}^{I*}, for each diabatic state are determined from a sampling function that is derived from (a) a Shannon entropy function[16,110,111] that depends on the initial quantum nuclear wavepacket density[14] and (b) an approximation to the potential energy surface associated with the quantum mechanical particle. Specifically, we employ the Shannon-entropy-based sampling function introduced in ref 16:

$$\omega(R_{\text{QM}}) \propto \frac{(\tilde{S}(R_{\text{QM}}) + 1)}{(\tilde{V}(R_{\text{QM}}) + 1)} \tag{B1}$$

where $\tilde{S}$ and $\tilde{V}$ are normalized to have values in $[0, 1]$. The Shannon entropy function corresponding to the nuclear wavepacket, $S[\rho(R_{\text{QM}})] \equiv -\rho \log(\rho)$, is a function of the wavepacket density: $\rho(R_{\text{QM}}) \equiv \chi^*(R_{\text{QM}}) \chi(R_{\text{QM}})$, which may be chosen on the basis of an estimate of the ground state from a reduced dimensional calculation. With the normalization stated above, $\tilde{S}[\rho(R_{\text{QM}})]$ and $\tilde{V}(R_{\text{QM}})$ have similar contributions toward the overall sampling function. The unit shifts in the numerator

and denominator of eq B1 retain numerical stability. The overall sampling functions, $\omega(R_{\text{QM}})$, is normalized according to

$$\|\omega(R_{\text{QM}})\|_1 = \int |\omega(R_{\text{QM}})| \, dR_{\text{QM}} = 1 \tag{B2}$$

This sampling function is derived from our time-dependent deterministic sampling (TDDS) approach[4,12,16] that has been used to improve the performance of QWAIMD calculations by several orders of magnitude with negligible loss in accuracy.[4] The sampling function above is utilized to locate the family of points $\{R_{\text{QM}}^{I*}\}$ that define $\mathbf{P}_I(\mathbf{R}_C; R_{\text{QM}}^{I*})$.

Once these significant points, $\{R_{\text{QM}}^{I*}\}$, are determined at the initial step of the dynamics, the quantized particle is placed on each of these grid points to compute a family of single particle electronic density matrices, $\{\mathbf{P}_I\}$. These, now, represent the diabatic states discussed in the previous section. Thus, the *I*th density matrix is chosen at the initial time step to be representative of the electronic structure at and around the nuclear configuration denoted by R_{QM}^{I*} and $\mathbf{R}_C$. Thus, each density matrix represents some local electronic structure on the quantum nuclear grid at the initial step. As the dynamics evolves through the Euler−Lagrange equations of motion derived from eq 4, these density matrices mix and the full potential surface is captured through the nonorthogonal CI formalism described above. Hence, the density matrices, $\mathbf{P}_I(\mathbf{R}_C; R_{\text{QM}}^{I*})$, are akin to "valence-bond" states.[77−81]

2. Combination of Atom-Centered and Adaptive-Mesh-Guided Gaussian Basis Functions To Simplify the On-the-Fly Potential Evaluations

As noted earlier, in contrast to conventional electronic structure approaches, the single-particle functions are expressed using a combination of atom-centered Gaussian basis functions and a set of Gaussians whose centers are localized on an adaptive spatial grid. That is, the diabatic density matrices, $\mathbf{P}_I(\mathbf{R}_C; R_{\text{QM}}^{I*})$ are expressed using a combination of atom-centered Gaussian basis functions (localized on the classical nuclei) and Gaussian primitives located on a chosen set of grid points that adapt to classical nuclear positions. There are two reasons for this hybrid basis choice: (a) The adaptive-mesh Gaussians are chosen to encompass the quantum nuclear grid. This is not only to allow accurate treatment of the delocalized electronic structure but also to eliminate the basis function dependence on the quantum-nuclear degrees of freedom. Thus, we retain atom-centered Gaussians basis functions on the classical nuclear degrees of freedom and substitute the same on the quantum nuclear subsystem with a band of basis functions that are located on an adaptive-mesh. This further enforces the independence of the diabatic states from the quantum nuclear degrees of freedom. (b) As a secondary source of computational gain, in ref 16 we have noted that for the hydrogen-bonded systems studied, fewer grid-based, adaptive Gaussians are required as compared to atom-centered Gaussians, with limited loss in accuracy. (See Table 2 in ref 16 for details.)

To determine the positions for the adaptive-mesh Gaussians, we use the recipe prescribed in ref 16, where these basis functions have been numerically benchmarked and found to provide results in agreement with higher level augmented, correlation-consistent series of atom-centered basis functions. Specifically, for Gaussian basis functions of the kind

$$\chi_{l,m,n}^{\mathbf{R}_F}(\mathbf{r}) = (x - R_x)^l (y - R_y)^m (z - R_z)^n \exp[-\alpha(\mathbf{r} - \mathbf{R}_F)^2] \tag{B3}$$

where the quantities l, m, and n are the usual orbital angular momentum indices of the basis function and the basis function centers, $\mathbf{R_F} [\equiv (R_x, R_y, R_z)]$, are chosen to be functions of multiple classical nuclear variables, i.e., $\mathbf{R_F} = f(\{\mathbf{R_C}\})$. For the case of hydrogen-bonded systems, we specialize our definition of $\mathbf{R_F} \equiv f(\{\mathbf{R_C}\})$ to a function of the donor and acceptor coordinates. The center for the ith Gaussian basis function is then given by

$$\mathbf{R_F}^i \equiv \sum_j c_{ji} \mathbf{R_C}^j + \vec{v}_i = a_i \mathbf{R_A} + d_i \mathbf{R_D} + \vec{v}_i \tag{B4}$$

where $\mathbf{R_A}$ and $\mathbf{R_D}$ are coordinate vectors of the donor and acceptor atoms for a hydrogen-bonded system and $\vec{v}_i$ is a uniform shift that can be used to create a three-dimensional band of electronic basis functions. It is further important to note that the basis functions introduced in eq B4 are functions of classical nuclear coordinates. Hence, in a fashion similar to atom-centered basis functions, the centers of these functions also transform according to the classical nuclear positions. Furthermore, these grid-based functions are spread uniformly in space. But these functions differ from plane-waves[112] through their $\{\mathbf{R_F}\}$ dependence of the Fourier transforms. The precise choice of the variables, $\{a_i, d_i, \vec{v}_i\}$, is discussed in section A. It may be noted that these grid-based Gaussian functions, when located using eq B4, may be thought of as a generalization to the bond-centered basis functions[113−116] traditionally used in quantum chemistry where the positions of these Gaussian basis functions are determined using the sampling function ω discussed above. However, in our case, we only require that $\mathbf{R_F} \equiv f(\{\mathbf{R_C}\})$.

As stated earlier, once basis functions are eliminated from quantum mechanical degrees of freedom, the diabatic states, $\{\mathbf{P}_I\}$, do not explicitly depend on the quantum nuclear grid position. This reinforces the diabatic nature of the states and leads to computational savings. Because there is no grid point dependence on the basis function, it is found that two-electron integrals can be reused over the entire quantum nuclear grid, which reduces the computational complexity in determining the diabatic state potential surfaces enormously. This approximation has been demonstrated to be accurate in ref 14 and is further tested in this publication.

■ AUTHOR INFORMATION

Corresponding Author
*S. S. Iyengar: e-mail, iyengar@indiana.edu.
Notes
The authors declare no competing financial interest.

■ ACKNOWLEDGMENTS

■ REFERENCES

(1) Hynes, J. T., Klinman, J. P., Limbach, H.-H., Schowen, R. L., Eds. *Hydrogen-Transfer Reactions*; Wiley-VCH: Weinheim, Germany, 2007.
(2) Isaacs, N. *Physical Organic Chemistry*; Longman Scientific and Technical: Essex, U.K., 1995.
(3) Sheridan, R. In *Reviews Of Reactive Intermediate Chemistry*; Platz, M., Moss, R. A., Maitland Jones, J., Eds.; Wiley-Interscience: Hoboken, NJ, 2007.
(4) Sumner, I.; Iyengar, S. S. *J. Phys. Chem. A* **2007**, *111*, 10313−10324.
(5) Swalina, C.; Hammes-Schiffer, S. *J. Phys. Chem. A* **2005**, *109*, 10410.
(6) Lopez, J. G.; McCoy, A. B. *J. Phys. Chem. A* **2006**, *110*, 5450−5457.
(7) Diken, E. G.; Headrick, J. M.; Roscioli, J. R.; Bopp, J. C.; Johnson, M. A.; McCoy, A. B.; Huang, X.; Carter, S.; Bowman, J. M. *J. Phys. Chem. A* **2005**, *109*, 571−575.
(8) McCoy, A. B.; Huang, X.; Carter, S.; Bowman, J. M. *J. Chem. Phys.* **2005**, *123*, 064317.
(9) Hammer, N. I.; Diken, E. G.; Roscioli, J. R.; Johnson, M. A.; Myshakin, E. M.; Jordan, K. D.; McCoy, A. B.; Huang, X.; Bowman, J. M.; Carter, S. *J. Chem. Phys.* **2005**, *122* (24), 244301.
(10) Iyengar, S. S.; Jakowski, J. *J. Chem. Phys.* **2005**, *122*, 114105.
(11) Iyengar, S. S. *Theor. Chem. Accts.* **2006**, *116*, 326.
(12) Jakowski, J.; Sumner, I.; Iyengar, S. S. *J. Chem. Theory Comput.* **2006**, *2*, 1203−1219.
(13) Sumner, I.; Iyengar, S. S. *J. Chem. Phys.* **2008**, *129*, 054109.
(14) Li, X.; Iyengar, S. S. *J. Chem. Phys.* **2010**, *133*, 184105.
(15) Li, X.; Iyengar, S. S. *J. Phys. Chem. A* **2011**, *115*, 6269.
(16) Hocker, D.; Li, X.; Iyengar, S. S. *J. Chem. Theory Comput.* **2011**, *7*, 256.
(17) Iyengar, S. S.; Sumner, I.; Jakowski, J. *J. Phys. Chem. B* **2008**, *112*, 7601−7613.
(18) Pacheco, A. B.; Iyengar, S. S. *J. Chem. Phys.* **2010**, *133*, 044105.
(19) Pacheco, A. B.; Iyengar, S. S. *J. Chem. Phys.* **2011**, *134*, 074107.
(20) Sumner, I.; Iyengar, S. S. *J. Chem. Theory Comput.* **2010**, *6*, 1698.
(21) Phatak, P.; Sumner, I.; Iyengar, S. S. *J. Phys. Chem. B* **2012**, *116*, 10145.
(22) Gerber, R. B.; Buch, V.; Ratner, M. A. *J. Chem. Phys.* **1982**, *77*, 3022.
(23) Gerber, R. B.; Ratner, M. A.; Buch, V. *Chem. Phys. Lett.* **1982**, *91*, 173.
(24) Buch, V.; Gerber, R. B.; Ratner, M. A. *Chem. Phys. Lett.* **1983**, *101*, 44.
(25) Bisseling, R. H.; Kosloff, R.; Gerber, R. B.; Ratner, M. A.; Gibson, L.; Cerjan, C. *J. Chem. Phys.* **1987**, *87*, 2760−2765.
(26) Tully, J. C. *Faraday Discuss.* **1998**, *110*, 407−419.
(27) Kapral, R.; Ciccotti, G. *J. Chem. Phys.* **1999**, *110*, 8919.
(28) Horenko, I.; Salzmann, C.; Schmidt, B.; Schutte, C. *J. Chem. Phys.* **2002**, *117*, 11075−11088.
(29) Donoso, A.; Zheng, Y. J.; Martens, C. C. *J. Chem. Phys.* **2003**, *119*, 5010.
(30) Brooksby, C.; Prezhdo, O. V. *Chem. Phys. Lett.* **2001**, *346*, 463−469.
(31) Prezhdo, O. V.; Brooksby, C. *Phys. Rev. Lett.* **2000**, *86*, 3215−3219.
(32) Gindensperger, E.; Meier, C.; Beswick, J. A. *J. Chem. Phys.* **2000**, *113*, 9369.
(33) Hammes-Schiffer, S.; Tully, J. C. *J. Chem. Phys.* **1994**, *101*, 4657.
(34) Li, R. *J. Sci. Comput.* **2005**, *24*, 321.
(35) Daubechies, I. *Ten Lectures in Wavelets*; SIAM: Philadelphia, PA, 1992.
(36) Strang, G.; Nguyen, T. *Wavelets and Filter Banks*; Cambridge Press: Cambridge, U.K., 1996.
(37) Strang, G.; Strela, V. *J. Opt. Eng.* **1994**, *33*, 2104−2107.
(38) Chan, Y. T. *Wavelet Basics*; Kluwer Academic Publishers: Norwell, MA, USA, 1995.
(39) Strang, G. *SIAM J. Numer. Anal.* **1968**, *5*, 506−516.
(40) Arias, T. *Rev. Mod. Phys.* **1999**, *71*, 267−311.
(41) Johnson, B. R.; Modisette, J. P.; Nordlander, P. J.; Kinsey, J. L. *J. Chem. Phys.* **1999**, *110*, 8309−8317.
(42) Iyengar, S. S.; Frisch, M. J. *J. Chem. Phys.* **2004**, *121*, 5061−5070.
(43) Kawaguchi, K. *J. Chem. Phys.* **1988**, *88*, 4186−4189.
(44) *High resolution spectroscopy*; John Wiley and Sons: New York, NY, 1998.
(45) Matsunaga, N.; Chaban, G. M.; Gerber, R. B. *J. Chem. Phys.* **2002**, *117*, 3541.
(46) Jung, J. O.; Gerber, R. B. *J. Chem. Phys.* **1996**, *105*, 10332−10348.
(47) Gerber, R. B.; Ratner, M. A. *J. Chem. Phys.* **1988**, *70*, 97−132.
(48) Bowman, J. M. *Acc. Chem. Res.* **1986**, *19*, 202−208.
(49) Kawaguchi, K.; Hirota, E. *J. Chem. Phys.* **1987**, *87*, 6838.
(50) Hunt, R. D.; Andrews, L. *J. Chem. Phys.* **1987**, *87*, 6819.
(51) McDonald, S. A.; Andrews, L. *J. Chem. Phys.* **1979**, *70*, 3134.

(52) Ault, B. S. *J. Phys. Chem.* **1979**, *83*, 837−844.

(53) Räsänen, M.; Seetula, J.; Kunttu, H. *J. Chem. Phys.* **1993**, *98*, 3194.

(54) Noble, P. N.; Pimentel, G. C. *J. Chem. Phys.* **1968**, *49*, 3165.

(55) Ault, B. S. *J. Chem. Phys.* **1979**, *83*, 837.

(56) Wight, C. A.; Ault, B. S.; Andrews, L. *J. Chem. Phys.* **1976**, *65*, 1244.

(57) Milligan, D. E.; Jacox, M. E. *J. Chem. Phys.* **1976**, *55*, 2550.

(58) Bondybey, V.; Pimentel, G. C.; Noble, P. N. *J. Chem. Phys.* **1971**, *55*, 540.

(59) Hirata, S.; Yagi, K.; Perera, S. A.; Yamazaki, S.; Hirao, K. *J. Chem. Phys.* **2008**, *128*, 214305.

(60) Baer, M. *Beyond Born-Oppenheimer: Conical Intersections and Electronic Nonadiabatic Coupling Terms*; Wiley: New York, 2006.

(61) Hanna, G.; Kapral, R. *Acc. Chem. Res.* **2006**, *39*, 21−27.

(62) Worth, G. A.; Cederbaum, L. S. *Annu. Rev. Phys. Chem.* **2004**, *55*, 127−158.

(63) Jasper, A. W.; Zhu, C.; Nangia, S.; Truhlar, D. G. *Faraday Discuss.* **2004**, *127*, 1−22.

(64) Kendrik, B. K.; Mead, C. A.; Truhlar, D. G. *Chem. Phys.* **2002**, *277*, 31−41.

(65) Kuppermann, A. In *Dynamics of Molecules and Chemical Reactions*; Wyatt, R. E., Zhang, J. Z. H., Eds.; Marcel Dekker Inc.: New York, NY, 1996; pp 411−472.

(66) Yarkony, D. R. *Rev. Mod. Phys.* **1996**, *68*, 985.

(67) Matsika, S.; Yarkony, D. R. *J. Am. Chem. Soc.* **2003**, *125*, 10672−10676.

(68) Szalay, P. G.; Müller, T.; Gidofalvi, G.; Lischka, H.; Shepard, R. *Chem. Rev.* **2012**, *112*, 108.

(69) Yamanaka, S.; Nishihara, S.; Nakata, K.; Yonezawa, Y.; Okumura, M.; Takada, T.; Nakamura, H.; Yamaguchi, K. *Int. J. Quantum Chem.* **2009**, *109*, 3811.

(70) Martin, R. L. *J. Chem. Phys.* **1981**, *74*, 1852.

(71) Voter, A. F.; Goddard, W. A., III. *Chem. Phys.* **1981**, *57* (3), 253−259.

(72) Jackels, C. F.; Davidson, E. R. *J. Chem. Phys.* **1976**, *64* (7), 2908−2917.

(73) Thom, A. J. W.; Head-Gordon, M. *J. Chem. Phys.* **2009**, *131* (12), 124113.

(74) Wu, Q.; Cheng, C.-L.; Van Voorhis, T. *J. Chem. Phys.* **2007**, *127*, 164119.

(75) Skone, J. H.; Pak, M. V.; Hammes-Schiffer, S. *J. Chem. Phys.* **2005**, *123*, 134108.

(76) Ayala, P. Y.; Schlegel, H. B. *J. Chem. Phys.* **1998**, *108*, 7560.

(77) Mulliken, R. S. *J. Chim. Phys.* **1964**, *61*, 20.

(78) Warshel, A.; Weiss, R. M. *J. Am. Chem. Soc.* **1980**, *102*, 6218.

(79) Chang, Y.-T.; Miller, W. H. *J. Phys. Chem.* **1990**, *94*, 5884.

(80) Borgis, D.; Staib, A. *Chem. Phys. Lett.* **1995**, *238*, 187.

(81) Day, T. J. F.; Soudachov, A. V.; Cuma, M.; Schmidt, U. W.; Voth, G. A. *J. Chem. Phys.* **2002**, *117*, 5839.

(82) Schlegel, H. B.; Millam, J. M.; Iyengar, S. S.; Voth, G. A.; Daniels, A. D.; Scuseria, G. E.; Frisch, M. J. *J. Chem. Phys.* **2001**, *114*, 9758−9763.

(83) Iyengar, S. S.; Schlegel, H. B.; Millam, J. M.; Voth, G. A.; Scuseria, G. E.; Frisch, M. J. *J. Chem. Phys.* **2001**, *115*, 10291−10302.

(84) Schlegel, H. B.; Iyengar, S. S.; Li, X.; Millam, J. M.; Voth, G. A.; Scuseria, G. E.; Frisch, M. J. *J. Chem. Phys.* **2002**, *117*, 8694−8704.

(85) Iyengar, S. S.; Schlegel, H. B.; Voth, G. A.; Millam, J. M.; Scuseria, G. E.; Frisch, M. J. *Isr. J. Chem.* **2002**, *42*, 191−202.

(86) Swope, W. C.; Andersen, H. C.; Berens, P. H.; Wilson, K. R. *J. Chem. Phys.* **1982**, *76*, 637−649.

(87) Amos, A. T.; Hall, G. G. *Proc. R. Soc. A* **1961**, *263*, 483.

(88) Löwdin, P.-O. *J. Appl. Phys.* **1962**, *33* (1), 251−280.

(89) King, H. F.; Stanton, R. E.; Kim, H.; Wyatt, R. E.; Parr, R. G. *J. Chem. Phys.* **1967**, *47*, 1936.

(90) Löwdin, P.-O. *Phys. Rev.* **1955**, *97* (6), 1474−1489.

(91) Löwdin, P.-O. *Phys. Rev.* **1955**, *97* (6), 1490−1508.

(92) Kouri, D. J.; Huang, Y.; Hoffman, D. K. *Phys. Rev. Lett.* **1995**, *75*, 49−52.

(93) Hoffman, D. K.; Nayar, N.; Sharafeddin, O. A.; Kouri, D. J. *J. Phys. Chem.* **1991**, *95*, 8299.

(94) Li, X.; Oomens, J.; Eyler, J. R.; Moore, D. T.; Iyengar, S. S. *J. Chem. Phys.* **2010**, *132*, 244301.

(95) Li, X.; Moore, D. T.; Iyengar, S. S. *J. Chem. Phys.* **2008**, *128*, 184308.

(96) Li, X.; Teige, V. E.; Iyengar, S. S. *J. Phys. Chem. A* **2007**, *111*, 4815−4820.

(97) Iyengar, S. S. *J. Chem. Phys.* **2005**, *123*, 084310.

(98) Iyengar, S. S. *J. Chem. Phys.* **2007**, *126*, 216101.

(99) Iyengar, S. S.; Petersen, M. K.; Day, T. J. F.; Burnham, C. J.; Teige, V. E.; Voth, G. A. *J. Chem. Phys.* **2005**, *123*, 084309.

(100) Iyengar, S. S.; Day, T. J. F.; Voth, G. A. *Int. J. Mass Spectrom.* **2005**, *241*, 197−204.

(101) Dietrick, S. M.; Pacheco, A. B.; Phatak, P.; Stevens, P. S.; Iyengar, S. S. *J. Phys. Chem. A* **2012**, *116*, 399−414.

(102) Pacheco, A. B.; Dietrick, S. M.; Stevens, P. S.; Iyengar, S. S. *J. Phys. Chem. A* **2012**, *116*, 4108.

(103) Press, W. H.; Teukolsky, S. A.; Vetterling, W. T.; Flannery, B. P. *Numerical Recipes In C*; Cambridge University Press: New York, 1992.

(104) Hanna, G.; Geva, E. *J. Phys. Chem. B* **2008**, *112* (41), 12991−13004.

(105) Mukamel, S. *Principles of Nonlinear Optical Spectroscopy*; Oxford, New York, 1995.

(106) Schmidt, J. R.; Corcelli, S. A.; Skinner, J. L. *J. Chem. Phys.* **2005**, *123*, 044513.

(107) Saven, J. G.; Skinner, J. L. *J. Chem. Phys.* **1993**, *99*, 4391.

(108) Golub, G. H.; Loan, C. F. V. *Matrix Computations*; The Johns Hopkins University Press: Baltimore, 1996.

(109) Helgaker, T.; Jørgensen, P.; Olsen, J. *Molecular Electronic-Structure Theory*; John Wiley and Sons, Ltd.: New York, 2000.

(110) Shannon, C. *Bell System Technical Journal* **1948**, *27*, 279−423.

(111) Shannon, C. *Proc. IEEE* **1998**, *86*, 447.

(112) Füsti-Molnar, L.; Pulay, P. *J. Chem. Phys.* **2002**, *116*, 7795.

(113) Rothenberg, S.; Schaefer, H. F., III. *J. Chem. Phys.* **1971**, *54*, 2764.

(114) Tao, F.-M.; Pan, Y.-K. *J. Chem. Phys.* **1992**, *97* (7), 4989−4995.

(115) Tao, F.-M. *J. Chem. Phys.* **1993**, *98* (3), 2481−2483.

(116) Williams, H. L.; Mas, E. M.; Szalewicz, K.; Jeziorski, B. *J. Chem. Phys.* **1995**, *103* (17), 7374−7391.

2280

dx.doi.org/10.1021/ct5002347 | *J. Chem. Theory Comput.* 2014, 10, 2265−2280